Strength testing under multi-axial stress states

A THESIS
SUBMITTED TO THE FACULTY OF THE GRADUATE SCHOOL
OF THE UNIVERSITY OF MINNESOTA
BY

Brian L. Folta

IN PARTIAL FULFILLMENT OF THE REQUIREMETNTS
FOR THE DEGREE OF
MASTER OF SCIENCE

Professor Joseph F. Labuz

June 2016

Acknowledgements

The work completed for this thesis would not have been possible without the assistance from several individuals and businesses. I would first like to thank professor Labuz for providing me with the opportunity to perform this work and offering his support throughout my research. Without his backing this thesis would not have been possible.

Setup of the experimental apparatus was possible in part because of the help of Paul Bergson and Mugurel Turos. Paul's assistance with the setup and running of the MTS load frame and Mugurel's insight during the design of the true-triaxial apparatus were important to the success of the device.

Several companies contributed to the completion of this research. Cold Spring Granite's donation of the Dunnville sandstone was very generous and greatly appreciated. The petrographic analysis provided by AET gave a greater understanding into the material being tested. MTS offered an explanation of the load frame and instrumentation, which helped the experiments run smoothly.

To perform experiments and data analysis, all colleagues of the rock mechanics lab made significant contributions. Ali Tarokh, Jacob Sharpe, Jianwen Peng, Feitao Zeng, and Yuan LI provided assistance in numerous forms and always created a great atmosphere that promoted quality research.

I would also like to thank my family for their constant support and encouragement. A special thank you to my parents, their continuing support and guidance were important for the completion of this research. Thank you to Kyle Rothmeyer for using his CAD expertise to generate detailed sketches of the apparatus. Finally, thank you to my fiancé Lindsey Gohr, her encouragement and patience provided the motivation and time needed to carry out this work.

Abstract

A true triaxial apparatus was designed and fabricated to apply mechanical loading to achieve multi-axial stress states. The University of Minnesota plane strain apparatus was equipped with piston assemblies that generated intermediate principal stress σ_{II} up to 100 MPa. The minor principal stress σ_{III} was limited by the pressure vessel to 24 MPa and the major principal stress σ_{I} was applied by a closed-loop, servo-hydraulic load frame. Calibration tests were conducted on an isotropic, linear elastic material (aluminum 6061) to confirm the performance of the piston assemblies.

Results from strength testing of Dunnville sandstone under multi-axial stress states were used to evaluate the Mohr-Coulomb (MC), Hoek-Brown (HB), and Paul-Mohr-Coulomb (PMC) failure criteria. A series of conventional triaxial compression ($\sigma_{II} = \sigma_{III}$) and extension ($\sigma_{I} = \sigma_{II}$) experiments were performed to evaluate the necessary material parameters for each failure criterion. The true triaxial apparatus was used to conduct experiments under various states of stress ($\sigma_{I} \neq \sigma_{II} \neq \sigma_{III}$) at constant mean stress ($p = \frac{\sigma_I+\sigma_{II}+\sigma_{III}}{3}$) of 28.3 and 56.0 MPa. The three criteria were compared in principal stress space on a plane normal to the hydrostatic axis called the pi-plane. Even though MC and HB are independent of σ_{II}, the stress states at failure were reasonably predicted at p = 28.3 MPa. This was not the case at p = 56.0 MPa, and a plane fitting method using a failure criterion such as PMC that includes σ_{II} may be needed.

Table of Contents

List of Tables

List of Figures

Chapter 1: Introduction

Design of a structure composed of or in rock requires a description of material response under a given state of stress. Material strength can be described through a failure criterion, which can be written in various forms depending on the analysis. A failure criterion can always be written in terms of three principal stresses ($\sigma_I \geq \sigma_{II} \geq \sigma_{III}$) and directions, where σ_I is the major, σ_{II} is the intermediate, and σ_{III} is the minor principal stress. If the material is isotropic, then the directional dependence can be eliminated and the principal stresses can be considered without order.

Many failure criteria, such as the popular Mohr-Coulomb or Hoek-Brown, only consider the effect of the major and minor principal stresses. However, material response can be affected by the intermediate principal stress. To examine this effect, criteria can be represented as a surface in principal stress space (cartesian coordinates σ_1, σ_2, σ_3). A section perpendicular to the hydrostatic axis ($\sigma_1 = \sigma_2 = \sigma_3$) called the π-plane can be considered. Investigating the effect of increasing intermediate stress at failure from $\sigma_{II} = \sigma_{III}$ to $\sigma_{II} = \sigma_I$ is possible when a criterion is displayed on the π-plane.

1.1 Compression testing with lateral confinement

The first notable compression test performed under combined axial and lateral stresses was by Adams and Nicolson (1901). A cylindrical rock specimen was placed inside a metal pipe and compressive axial load applied. As axial stress increased, lateral displacement increased causing lateral stress to be applied to the specimen. Two significant qualitative observations were made from the addition of lateral confinement: (1) Axial load at failure increased and (2) ductile behavior increased. Quantitative results were not obtained due to the difficulty of estimating lateral stresses and frictional effects between the pipe wall and specimen.

Quantitative results from triaxial experiments were obtained from the work of von Kàrmàn in 1911. In von Karman's experiments, the specimen was jacketed and lateral stress was applied with fluid pressure through the use of a high pressure vessel (Mogi 2007). Unlike the experiments performed by Adams and Nicolson (1901), a nearly homogeneous stress state was produced within the specimen permitting the accurate measurement of stress and strain. The stress state in both Adams and Nicolson and von Kàrmàn's experiments was $\sigma_1 > \sigma_2 = \sigma_3$ and is referred to as conventional triaxial compression.

Another significant step in triaxial testing occurred when Böker in 1915 performed experiments in which confining pressure was larger than axial stress ($\sigma_1 < \sigma_2 = \sigma_3$) (Mogi 2007). Using this stress state, referred to as conventional triaxial extension, the specimen was elongated in the axial direction inducing failure under extension through the application of only compressive normal stresses. After Böker, a number of experiments were carried out under conventional triaxial compression or extension.

1.2 True triaxial compression testing

Starting around 1960, different experimental methods were developed to explore the role of all three principal stresses. Devices were designed to independently apply each principal stress ($\sigma_1 \geq \sigma_2 \geq \sigma_3$). To experimentally achieve this stress state, several approaches will be discussed. Testing methods are categorized as indirect and direct, indirect meaning constitutive relationships must be used to calculate stresses and direct meaning only equilibrium is needed to determine stresses.

1.2.1 Indirect multi-axial testing

Experiments have been performed on hollow cylindrical specimens, both thick and thin walled. Platens were attached to the ends of the cylinder and the specimen was jacketed. Axial stress was applied through the platens and confining pressure was applied in the lateral direction (Fig. 1). The experiments were carried out by maintaining internal and external pressure constant, and

bringing the specimen to failure through increasing axial stress. The radial and tangential stresses, σ_r and σ_θ, can be indirectly calculated using the Lame solution:

$$\sigma_r = \frac{r_i^2 p_i - r_o^2 p_o}{r_o^2 - r_i^2} + \frac{r_i^2 r_o^2 (p_o - p_i)}{r^2 (r_o^2 - r_i^2)} \quad (1)$$

$$\sigma_\theta = \frac{r_i^2 p_i - r_o^2 p_o}{r_o^2 - r_i^2} - \frac{r_i^2 r_o^2 (p_o - p_i)}{r^2 (r_o^2 - r_i^2)} \quad (2)$$

where

$r_i = cylinder\ inner\ radius$

$r_o = cylinder\ outer\ radius$

From equations (1) and (2), it can be seen that for constant r_i and r_o, different σ_r and σ_θ values can be achieved through variation of p_i and p_o. Experiments performed by Hoskins (1969) and Robertson (1955) were accomplished using thick walled cylinders. However, inhomogeneous stress distributions are produced within the walls of the specimens. Both σ_r and σ_θ change in magnitude from the inner to outer radius of the cylinder. The effect of this stress gradient on rock strength is unknown. Also, because elasticity does not apply as failure is reached the principal stresses could be different than the stresses calculated from equations (1) and (2).

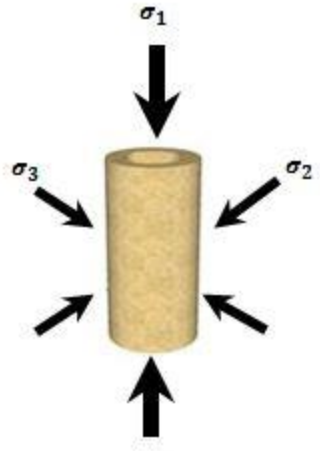

Figure 1: Hollow cylinder with axial compression and confining pressure

Efforts were made by Handin et al. (1967) to improve upon the thick walled cylinder design. By using a thin walled (wall thickness < 0.7 mm) hollow cylinder allowed for a nearly homogeneous stress state distribution. Using the thin walled hollow cylinder under the same configuration as Hoskins and Robertson, three different principal stresses were again achieved. While it was shown that a true triaxial stress condition was achievable, the authors noticed one shortcoming of their method: reproducibility was difficult.

1.2.2 Direct compression using three platens

Multiple experimental devices have been built in which stress is applied using hydraulic actuators with three pairs of platens (Fig. 2) (Niwa et al. 1967, Hunsche & Albrecht, 1990). When using this type of true triaxial device an important consideration is minimizing the frictional effects at the contact between specimen and platens. A typical method to reduce frictional effects is though lubrication of the platen-specimen contact. However, different lubrications may cause different boundary conditions, affecting failure strength (Mogi 2007).

Multi-axial testing using three platens has been used to investigate rock strength under polyaxial stress at elevated temperatures (Hunsche & Albrecht, 1990). In

these experiments, specimens were first loaded hydrostatically to a desired mean stress. Deviatoric load was then applied to bring about failure. The deviatoric load was applied by changing all three principal stresses so that mean stress remained constant. The use of hydraulic actuators and three platens is a well suited experimental method for constant mean stress testing.

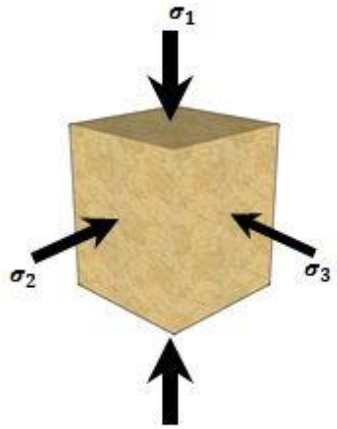

Figure 2: Compression using three platens

1.2.3 Direct compression using one platen and fluid pressure

True triaxial cells have been developed in which maximum axial stress (σ_1) is applied through a platen, and lateral stresses (σ_2 and σ_3) are applied using two different fluid pressures (Fig. 3). Applying stress with two independent fluid pressures is difficult, so methods have been devised to mimic the application of fluid pressures. In the cell developed by Hojem and Cook (1968), σ_1 is applied through a platen and σ_2 and σ_3 are applied through “soft” copper flat jacks. Due to the soft nature of the copper flat jacks it is claimed that pressure is transferred to the specimen similar to fluid pressure. A major limiting factor to this design is the strength of the copper flat jacks. The desirable “soft” quality of the flat jacks also creates a major limitation in the stress applied in the lateral direction, typically no larger than 50 MPa.

Mogi (1977) performed a variation of this direct multi-axial method. Axial stress (σ_1) was applied through a solid platen, intermediate lateral stress (σ_2) was applied through soft rubber, and minimum lateral stress (σ_3) was applied by fluid confining pressure.

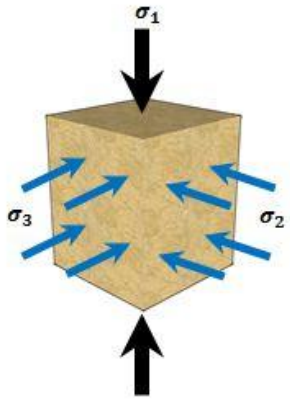

Figure 3: Compression using one platen and fluid pressure

1.2.4 Direct compression using two platens and fluid pressure

A true triaxial device was developed using two steel platens to apply σ_1 and σ_2, and confining pressure to apply σ_3 (Fig. 4) (Mogi 1969, 1970). Major principal stress (σ_I) was applied with a piston of capacity 700 kN, and intermediate principal stress (σ_{II}) was applied with a piston of capacity 300 kN. The apparatus contained a thick walled pressure vessel allowing the application of the minor principal stress (σ_{III}). The minor principal stress has a large influence on failure of rock. Using fluid pressure to apply σ_3, a homogeneous stress state was achievable up to very high stresses (σ_3 > 800 MPa) when compared to application of stress with three platens (Mogi 2007). Specimens tested in Mogi's apparatus were rectangular prisms of dimension 1.5 x 1.5 x 3.0 cm.

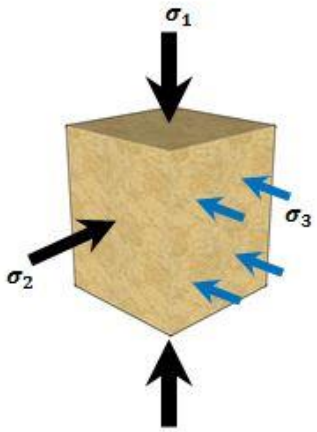

Figure 4: Compression using two platens and fluid pressure

A cell similar to Mogi's, with the ability to test a larger specimen, was built by Takahashi and Koide (1989). Specimens tested in this apparatus were rectangular prisms of dimension 3.5 x 3.5 x 7.0 cm. Minor principal stress, which was applied with fluid pressure, was much lower than Mogi's at a maximum of 50 MPa. It was found that for certain rock, Shirahama sandstone and Yuubari shale, while peak strength is influenced by intermediate stress, residual strength shows little dependence on intermediate stress (Takahashi & Koide 1989).

Two true triaxial devices were constructed at Sandia National Lab (Wawersik et al. 1997). Both devices are similar, however the larger cell has more features and will only be discussed. As is common, axial force was provided through a fixed axial base platen and a movable top piston. Lateral loading jacks reacting against the pressure vessel walls provided stress in the intermediate direction. The pressure vessel facilitated the application of fluid confining pressure in the minor lateral direction up to $\sigma_3 = 100$ MPa. The pressure vessel has an inside diameter of 17.8 cm and could accommodate specimens up to 7.6 x 7.6 x 17.8 cm. This cell has been used to assess the influence of the intermediate principal stress on mechanical response and failure (Ingraham et al. 2013).

Capabilities of this device included testing of larger specimens, application of pore pressure and fluid flow, and generation of large axial strain (up to 15%). Pore pressure was allowed through ports placed in the top and bottom axial loading platens. To allow for large axial strains, the generation of inhomogeneous stress distributions needed to be minimized. To do this, a system was developed to ensure that the center of the lateral loading pistons and center of the specimen always remained equal height (Wawersik et al. 1997).

Haimson et al. (2000) developed another variation of this type of direct multi-axial testing device. An important feature of this device is its ability to apply very large compressive stresses ($\sigma_3 = 400\ MPa$). Minor principal stress is applied through confining pressure and major and intermediate stresses are applied through solid platens. This device uses two sets of orthogonal pistons seated inside a biaxial apparatus to apply σ_1 and σ_2. A unique feature of this device is that it does not require a compression-testing device to apply any of the principal stresses, making it relatively portable (Haimson et al. 2000).

1.3 Objectives

The objectives of this thesis are to review the formulation of the Mohr-Coulomb, Hoek-Brown, and Paul-Mohr-Coulomb criteria in different coordinate systems. The coordinate systems used are the σ_1-σ_3 plane, p-q plane, and the π-plane of principal stress space. A formulation for each criterion is presented in each of the coordinate systems. Conventional compression and extension testing was performed to determine the material parameters necessary for construction of each failure surface. A true-triaxial apparatus was designed and fabricated. Multi-axial tests were performed to provide results in the π-plane for evaluation of the three failure criteria.

1.4 Organization

Chapter 2 presents the formulation of the Mohr-Coulomb, Hoek-Brown, and Paul-Mohr-Coulomb criterion in three coordinate systems. It also presents a fitting method for construction of the Paul-Mohr-Coulomb criteria. A description of the experiments performed and the material tested is given in Chapter 3. Development of a true triaxial apparatus is also discussed. In Chapter 4 material strengths parameters are given and each criterion compared against the experimental results. A discussion of results and future developments is given in Chapter 5.

Chapter 2: Background on failure criteria

Design of a structure composed of rock requires a description of material failure through a failure criterion, which should be verified from experimental results obtained from multi-axial strength tests. A failure criterion can be written in terms of three principal stresses (σ_I, σ_{II}, σ_{III}) and three directions. If the rock is isotropic, then the directional dependence disappears and the criterion can always be written as:

$$f(\sigma_1, \sigma_2, \sigma_3) = 0 \tag{3}$$

where σ_1, σ_2, and σ_3 are principal stresses with no regard to order

It is often convenient to represent a failure criterion using different coordinate systems. Three coordinate systems will be introduced in this chapter for three different failure criteria. One way a failure criterion can be represented is as a line in the σ_1-σ_3 plane, the shape of the surface being defined by the form of equation (3). A linear equation plots as a line in the σ_1-σ_3 plane and a nonlinear equation plots as a curvilinear surface (Paul 1968; Drescher 1991).

Failure criterion can also be represented in terms of the stress invariants p and q:

$$p = \frac{1}{3}(I_1) = \frac{1}{3}(\sigma_1 + \sigma_2 + \sigma_3) \tag{4}$$

$$q = \sqrt{3J_2} = \sqrt{\frac{1}{2}[(\sigma_1 - \sigma_2)^2 + (\sigma_2 - \sigma_3)^2 + (\sigma_3 - \sigma_1)^2]} \tag{5}$$

where

I_1 is the first stress invariant

J_2 is the second stress invariant of the deviator stress, $S_{ij} = \sigma_{ij} - p\delta_{ij}$

Equations (4) and (5) can be simplified for the conventional triaxial condition. Due to the nature in which rock is sampled, right cylindrical cores, a typical method of testing is conventional triaxial testing. The stress state in triaxial experiments is an axial stress σ_a applied along the longitudinal axis of the specimen and radial

stress σ_r applied by confining pressure. During triaxial compression, the stress state is $\sigma_I = \sigma_a$ and $\sigma_{II} = \sigma_{III} = \sigma_r$. The stress state during triaxial extension is $\sigma_{III} = \sigma_a$ and $\sigma_I = \sigma_{II} = \sigma_r$. The invariants p and q for conventional triaxial testing are simply:

$$p = \frac{1}{3}(\sigma_a + \sigma_r + \sigma_r) = \frac{1}{3}(\sigma_a + 2\sigma_r) \tag{6}$$

$$q = \sqrt{\frac{1}{2}[(\sigma_a - \sigma_r)^2 + (\sigma_r - \sigma_r)^2 + (\sigma_r - \sigma_a)^2]} = \sigma_a - \sigma_r \tag{7}$$

From equation (7), the value of q will either be positive or negative depending on the triaxial experiment performed. For triaxial compression when $\sigma_a > \sigma_r$ then $q > 0$ and for triaxial extension when $\sigma_a < \sigma_r$ then $q < 0$.

Any failure criterion can also be presented in principal stress space, and one view is on a plane perpendicular to the hydrostatic axis ($\sigma_1 = \sigma_2 = \sigma_3$) called the π-plane described by:

$$p = \frac{\sigma_1 + \sigma_2 + \sigma_3}{3} = constant \tag{8}$$

Because there are six possible orderings of the principal stresses, equation (3) actually represents six failure surfaces. Each failure surface corresponds to a particular order of the principal stresses. An example failure surface for a pressure-dependent material is a pyramidal failure surface with a common vertex V_0 on the tension side of the hydrostatic axis (Fig. 5a). The failure surface in the π-plane displays a three-fold symmetry where the axes σ_1', σ_2', and σ_3' are the projections of the coordinate axes. Thus, any one of the 60° sections (Fig. 5b) uniquely defines a failure surface (Paul 1968). In order to construct a failure surface in the π-plane, all planes must intersect at a theoretical uniform triaxial tensile strength V_0 on the p-axis.

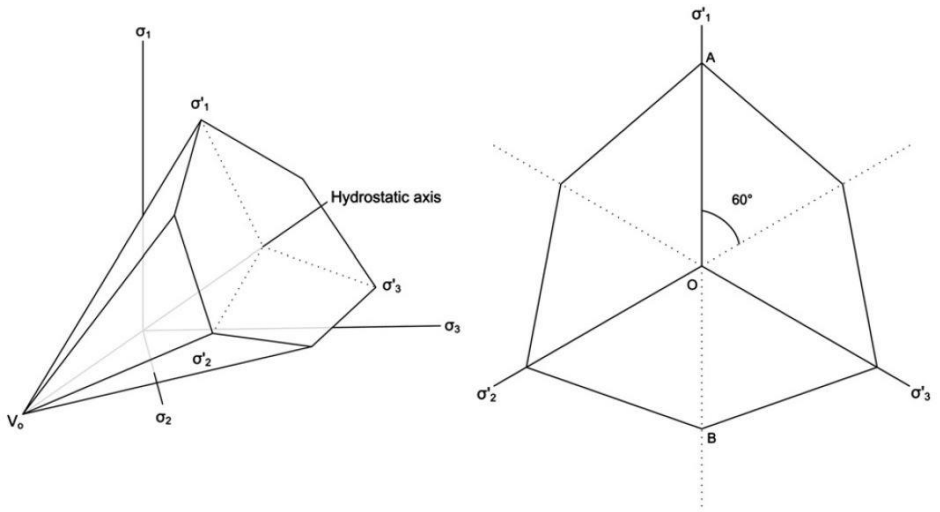

Figure 5: a) Six-sided pyramidal failure surface (left). b) Section in π-plane(right) (Meyer and Labuz 2013)

Any point in principal stress space can be represented in terms of $(\sigma_1, \sigma_2, \sigma_3)$. To construct a surface in the π-plane the following procedure is used. Point M on the π-plane can be presented as M(r, θ, p) in polar coordinates as long as $r \geq 0$ (Fig. 6a). At a constant p, the point M has a distance *r* from the hydrostatic axis and is oriented at an angle θ from the σ_1' axis. The length along the σ_1' axis to point M is rcos(θ). To determine how point M can be written in terms principal stresses a cross-section along the hydrostatic axis and intersecting the σ_1 axis is drawn (Fig. 6b). The hydrostatic axis intersects each of the principal stress axes at an angle β, such that $\cos(\beta) = \frac{1}{\sqrt{3}}$ and $\sin(\beta) = \frac{\sqrt{6}}{3}$. Knowing the value of β, for a constant p the principal coordinate σ_1 for point M can be written as:

$$\sigma_1 = p + rcos(\theta)\sin(\beta) \tag{9}$$

Equation (9) simplifies to:

$$\sigma_1 = p + \frac{\sqrt{6}}{3} rcos(\theta) \tag{10}$$

To obtain the equations for σ_2 and σ_3 for point M, a similar process can be followed by drawing cross-sections intersecting the hydrostatic axis and the σ_2 and σ_3 axes. The remaining two equations become:

$$\sigma_2 = p - \frac{\sqrt{6}}{3} r sin\left(\frac{\pi}{6} + \theta\right) \quad (11)$$

$$\sigma_3 = p - \frac{\sqrt{6}}{3} r sin\left(\frac{\pi}{6} - \theta\right) \quad (12)$$

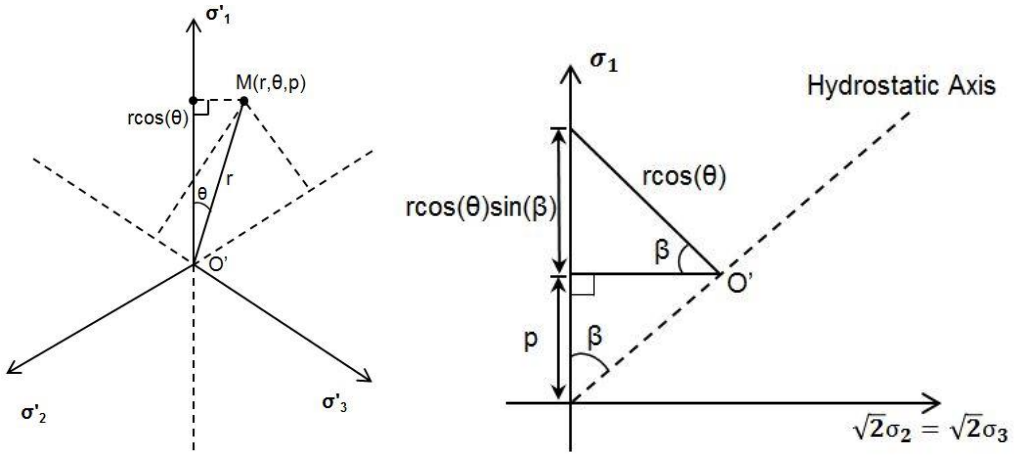

Figure 6: a) π-plane section (left) b) Cross-section along hydrostatic axis (right)

Equations (10-12) can be used to construct a π-plane surface for linear and nonlinear failure criteria. Given the equation for a failure criterion in terms of principal stresses and knowing the correct ordering of the principal stresses in each π-plane section, simply plugging equations (10-12) into the failure criterion will allow for construction of the π-plane surface.

This chapter will look into the formulation of the Mohr-Coulomb, Hoek-Brown, and Paul-Mohr-Coulomb failure criteria in the σ_1-σ_3 plane, p-q plane, and π-plane associated with $\sigma_1, \sigma_2, \sigma_3$.

2.1 Mohr-Coulomb

The Mohr Coulomb (MC) failure criterion is one of the most widely used theories for describing rock failure. The MC criterion is a set of linear equations in principal stress space that represent failure of an isotropic material with no effect of intermediate principal stress (σ_{II}). When expressed in terms of principal stresses, the MC criterion has the following form:

$$\sigma_I = K_p \sigma_{III} + C_0 \quad (13)$$

where

$$K_p = \frac{1 + sin\phi}{1 - sin\phi}$$

$$C_0 = \frac{2ccos\phi}{1 - sin\phi}$$

K_p is the slope of the compression line and is related to the friction angle. C_0 is the uniaxial compression strength and is related to cohesion and friction angle. Figure 7 shows the MC failure criterion in the σ_1-σ_3 plane. The MC criterion can be written for conventional triaxial compression by substituting $\sigma_a = \sigma_I$ and $\sigma_r = \sigma_{III}$ into equation (13):

$$\sigma_a = K_p \sigma_r + C_0 \quad (14)$$

Similarly for extension:

$$\sigma_r = K_p \sigma_a + C_0 \quad (15)$$

It is convenient to write the extension condition as $\sigma_a = F(\sigma_r)$:

$$\sigma_a = \frac{\sigma_r}{K_p} - \frac{C_0}{K_p} = \sigma_r \frac{1}{K_p} - T_0 \quad (16)$$

Construction of a failure surface in principal stress space requires all planes to intersect at one point referred to as the vertex (V_0) or uniform triaxial tensile strength. Using MC, V_0 can be directly calculated and has the following relationship to the compression line slope (K_p) and uniaxial compressive strength (C_0). By substituting $\sigma_a = -V_0$ and $\sigma_r = -V_0$ into equations (14) or (15) the MC criterion can be written as:

$$-V_0 = K_p(-V_0) + C_0 \quad (17)$$

Rearranging it is shown that V_0 equals:

$$V_0 = \frac{C_0}{K_p - 1} \tag{18}$$

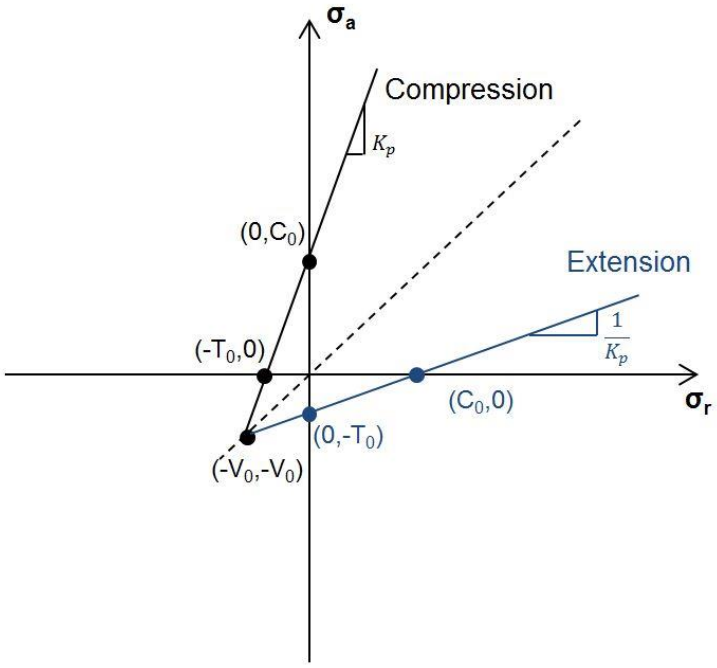

Figure 7: MC in compression and extension in the σ_1-σ_3 plane

To formulate MC in the p-q plane the following procedure was used. Plugging in the coefficients K_p and C_0 and rearranging, equation (13) becomes:

$$(\sigma_I - \sigma_{III}) = (\sigma_I + \sigma_{III})sin\phi + 2ccos\phi \tag{19}$$

For a conventional triaxial compression test equation (19) can be written as:

$$(\sigma_a - \sigma_r) = (\sigma_a + \sigma_r)sin\phi + 2ccos\phi \tag{20}$$

Expanding and rearranging equation (20) becomes:

$$(\sigma_a - \sigma_r)(3 - sin\phi) = 2(\sigma_a + 2\sigma_r)sin\phi + 6ccos\phi \tag{21}$$

Equations (6) and (7) can be substituted in equation (21):

$$q(3 - sin\phi) = 6psin\phi + 6ccos\phi \tag{22}$$

Rearranging equation (22) the MC failure criterion for triaxial compression can be written as:

$$q = \frac{6sin\phi}{3 - sin\phi}p + \frac{6ccos\phi}{3 - sin\phi} \tag{23}$$

A similar process can be followed for extension:

$$q = -\frac{6sin\phi}{3 + sin\phi}p - \frac{6ccos\phi}{3 + sin\phi} \tag{24}$$

Figure 8 shows a sketch of the MC criterion in p-q plane. Equations (23) and (24) can be written as:

$$q = m_{c,e}p + b_{c,e} \tag{25}$$

where the subscripts denote a compression or extension failure condition

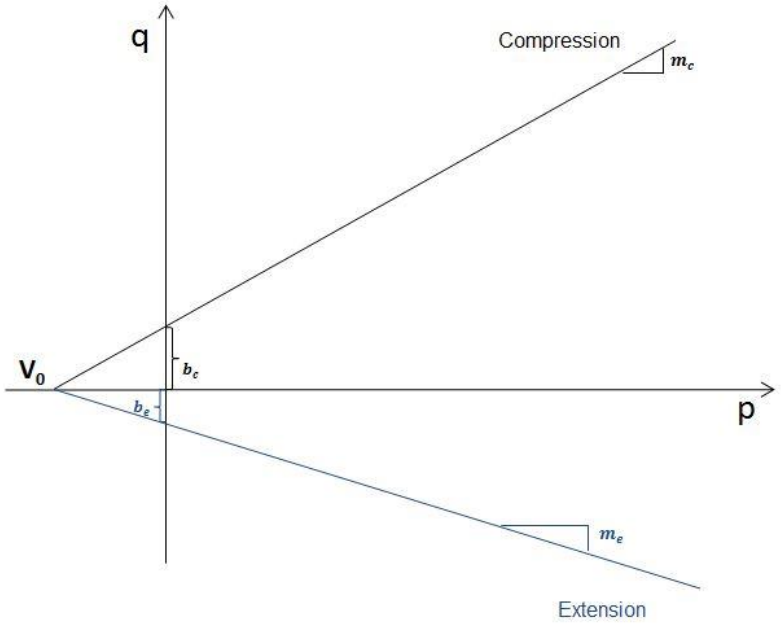

Figure 8: MC compression and extension in the p-q plane

A π-plane can be constructed using the MC criterion (Fig. 9). Section one of the π-plane has an ordering of principal stress of $\sigma_1 > \sigma_2 > \sigma_3$. To construct the section one surface, equations (10) and (12) are substituted into (13) to get an equation describing the section line. Similarly, to construct failure surfaces in all the sections, substituting the correct order of equations (10-12) into (13) will yield an equation describing the failure surface.

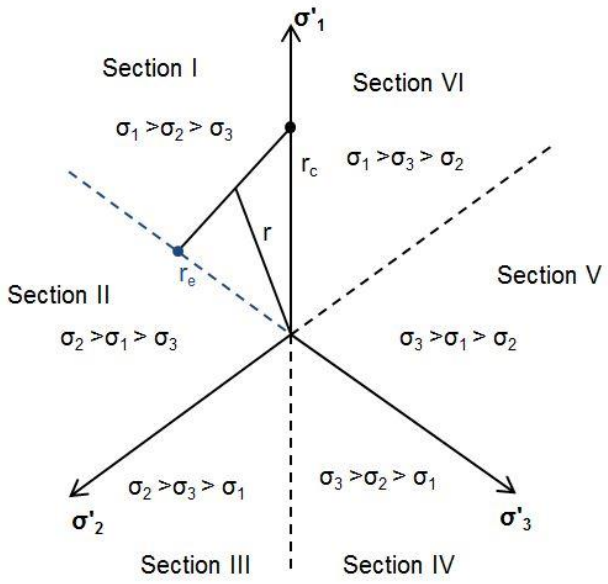

Figure 9: MC π-plane with section six constructed

2.2 Hoek-Brown

Hoek-Brown (HB) is a non-linear criterion in principal stress space that describes an increase of peak strength with confining stress for isotopic rock with no effect of intermediate stress (σ_{II}) (Eberhardt 2012). The HB criterion can be expressed in terms of principal stresses through the following equation:

$$\sigma_I = \sigma_{III} + C_0 \sqrt{m \frac{\sigma_{III}}{C_0} + 1} \tag{26}$$

where

$C_0 = uniaxial\ compression\ strength$

$m = fitting\ parameter\ based\ on\ rock\ type$

The HB criterion can be written for conventional triaxial compression by substituting $\sigma_a = \sigma_I$ and $\sigma_r = \sigma_{III}$ into equation (26):

$$\sigma_a = \sigma_r + C_0 \sqrt{m \frac{\sigma_r}{C_0} + 1} \tag{27}$$

The same process can be followed for the extension condition by substituting $\sigma_a = \sigma_{III}$ and $\sigma_r = \sigma_I$ into equation (26):

$$\sigma_r = \sigma_a + C_0 \sqrt{m \frac{\sigma_a}{C_0} + 1} \tag{28}$$

It is convenient to write the extension condition as $\sigma_a = F(\sigma_r)$:

$$\sigma_a = \sigma_r - \frac{\sqrt{4mC_0\sigma_r + (m^2C_0^2 + 4C_0^2)} - mC_0}{2} \tag{29}$$

Figure 10 shows a sketch of the compression and extension H-B failure surfaces. It can be shown the uniform triaxial tensile strength (V_0) has the following relationship to the fitting parameter (m) and uniaxial compressive strength (C_0). By substituting $\sigma_a = -V_0$ and $\sigma_r = -V_0$ equation (27) or (28) becomes:

$$-V_0 = -V_0 + C_0 \sqrt{m \frac{-V_0}{C_0} + 1} \tag{30}$$

Rearranging equation (30):

$$(-V_0 - (-V_0))^2 = C_0^2 \left(m \frac{-V_0}{C_0} + 1 \right) \tag{31}$$

Simplifying (31) gives the following form for V_0:

$$V_0 = \frac{C_0}{m} \tag{32}$$

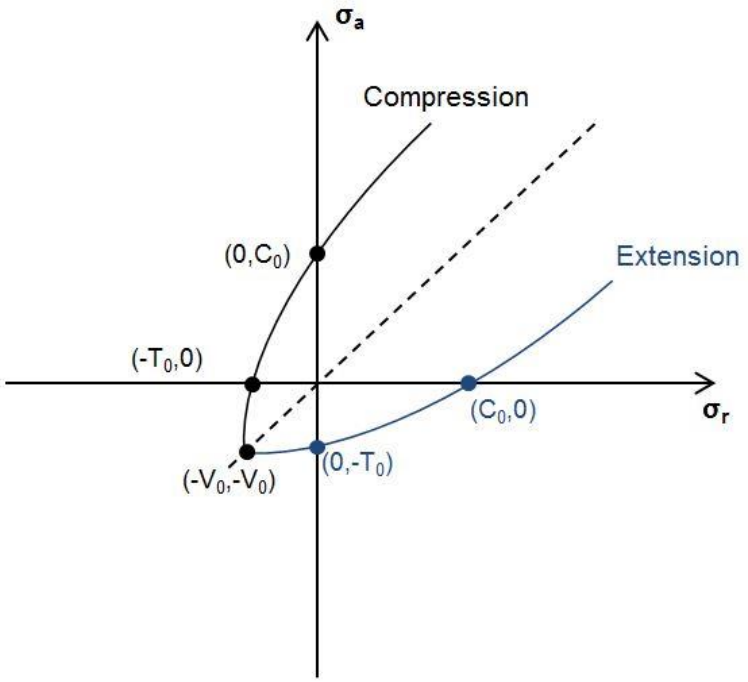

Figure 10: HB compression and extension in the $\boldsymbol{\sigma_1}$-$\boldsymbol{\sigma_3}$ plane

To express HB in the p-q plane, equation (26) can be rearranged:

$$(\sigma_I - \sigma_{III})^2 + {C_0}^2 \left(m \frac{\sigma_{III}}{C_0} + 1 \right) \tag{33}$$

For conventional triaxial compression equation (33) can be rewritten knowing $\sigma_a = \sigma_I$ and $\sigma_r = \sigma_{III}$:

$$(\sigma_a - \sigma_r)^2 + {C_0}^2 \left(m \frac{\sigma_r}{C_0} + 1 \right) \tag{34}$$

The stress invariants p and q from equations (6) and (7) can be rearranged and written as:

$$\sigma_a = 3p - 2\sigma_r \tag{35}$$

$$\sigma_a = q + \sigma_r \tag{36}$$

Subtracting (36) from (35) gives:

$$\sigma_a - \sigma_a = 3p - 2\sigma_r - (q + \sigma_r) = \sigma_r = \frac{3p - q}{3} \tag{37}$$

Using equations (7) and (37) in (34) the HB criterion for compression in the p-q plane becomes:

$$q^2 = {C_0}^2 \left(\frac{m}{C_0}\frac{3p-q}{3} + 1\right) \tag{38}$$

Rearranging:

$$q^2 = C_0 m \left(\frac{3p-q}{3}\right) + {C_0}^2 \tag{39}$$

A similar process can be followed for extension:

$$q^2 = C_0 m \left(p - \frac{2}{3}q\right) + {C_0}^2 \tag{40}$$

Both equations (39) and (40) are implicit equations. Solving the roots of equation (39) gives:

$$q = \frac{1}{6}\left(\pm\sqrt{C_0}\sqrt{C_0 m^2 + 36C_0 + 36mp} - C_0 m\right) \tag{41}$$

Solving the roots of equation (40) gives:

$$q = \frac{1}{3}\left(\pm\sqrt{C_0^2 m^2 + 9C_0^2 + 9C_0 mp} + C_0 m\right) \tag{42}$$

The positive root of equation (41) and the negative root in equation (42) are used to plot the failure surface. Equations (41) and (42) do not have the same form, therefore HB is asymmetric in the p-q plane. A sketch of the HB criterion is shown in Figure 11.

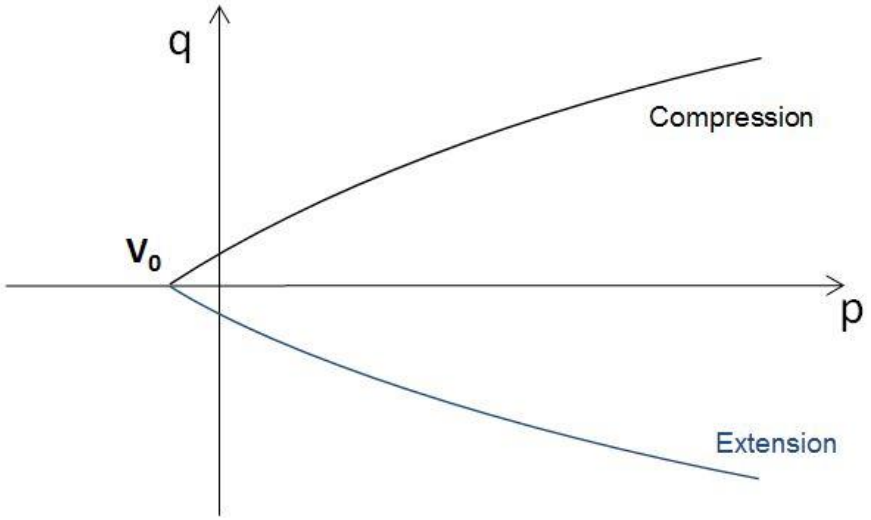

Figure 11: HB compression and extension in p-q plane

Non-linear failure criteria, such as HB, can be used to represent a failure surface in the π-plane. To formulate HB in the π-plane the expressions for principal stresses (10-12) were used. Looking again at section one, plugging in equations (10) and (12) into (26) an equation describing the HB criterion for the principal stress ordering $\sigma_1 > \sigma_2 > \sigma_3$ is obtained (Fig. 12). Similarly, to construct failure surfaces in all the sections substituting the correct order of equations (10-12) into (26) will yield an equation describing the surface in each section. The failure surface in Figure 12 is exaggerated to show the nonlinearity of HB; however, it is nearly a line.

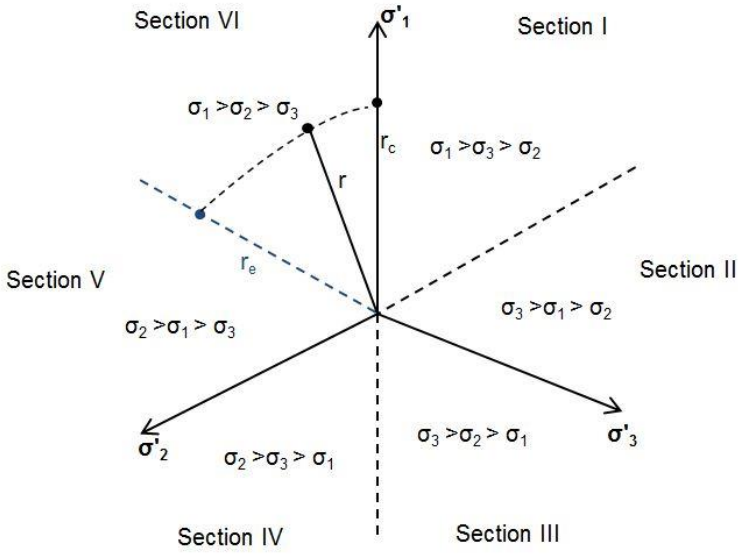

Figure 12: HB criterion in the π-plane

2.3 Paul-Mohr-Coulomb

Paul-Mohr-Coulomb (PMC) is a linear multi-axial failure criterion in which the intermediate principal stress influences failure. PMC can be written in terms of principal stresses using the following general equation:

$$A\sigma_I + B\sigma_{II} + C\sigma_{III} = 1 \tag{43}$$

Or in terms of strength parameters and the vertex (V_0) (Meyer and Labuz 2013):

$$\frac{\sigma_I}{V_0}\left[\frac{1-sin\phi_c}{2sin\phi_c}\right] + \frac{\sigma_{II}}{V_0}\left[\frac{sin\phi_c - sin\phi_e}{2sin\phi_c sin\phi_e}\right] - \frac{\sigma_{III}}{V_0}\left[\frac{1+sin\phi_e}{2sin\phi_e}\right] = 1 \tag{44}$$

The subscripts c and e denote a condition of compression and extension. To formulate PMC in the σ_1-σ_3 plane, first consider the conventional triaxial compression stress state ($\sigma_{II} = \sigma_{III} = \sigma_r$ and $\sigma_I = \sigma_a$):

$$\frac{\sigma_a}{V_0}\left[\frac{1-sin\phi_c}{2sin\phi_c}\right] + \frac{\sigma_r}{V_0}\left[\frac{sin\phi_c - sin\phi_e}{2sin\phi_c sin\phi_e}\right] - \frac{\sigma_r}{V_0}\left[\frac{1+sin\phi_e}{2sin\phi_e}\right] = 1 \tag{45}$$

Equation (45) can be simplified to the following form:

$$\sigma_a = \frac{1 + sin\phi_c}{1 - sin\phi_c}\sigma_r + \frac{2c_c cos\phi_c}{1 - sin\phi_c} \quad (46)$$

Similarly for conventional triaxial extension when $\sigma_I = \sigma_{II} = \sigma_r$ and $\sigma_{III} = \sigma_a$ PMC can be written as:

$$\sigma_r = \frac{1 + sin\phi_e}{1 - sin\phi_e}\sigma_a + \frac{2c_e cos\phi_e}{1 - sin\phi_e} \quad (47)$$

Or more generally in the form:

$$\sigma_I = M_{c,e}\sigma_{III} + C_{c,e} \quad (48)$$

where

$$M_{c,e} = \frac{1 + sin\phi_{c,e}}{1 - sin\phi_{c,e}}$$

$$C_{c,e} = \frac{2c_{c,e} cos\phi_{c,e}}{1 - sin\phi_{c,e}}$$

To plot PMC in the σ_1-σ_3 plane equation (44) is used for the compression line and equation (47) for the extension line (Fig.13). Unlike the MC criterion, PMC is not symmetric because the slopes in compression and extension depend on friction angles of different values. Fitting a line of least-squares to extension and compression data independently will yield two unequal intercepts with the dashed axis (Fig. 13). A fitting method to determine V_0 will be discussed.

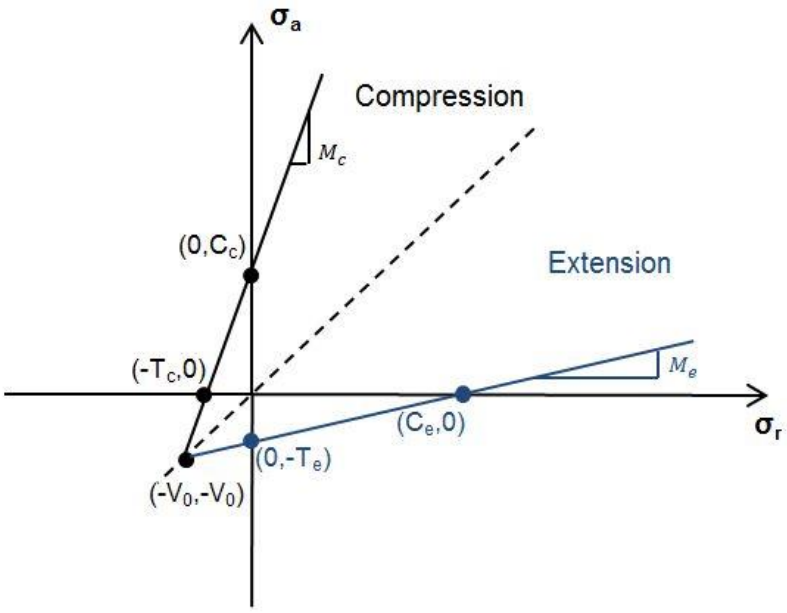

Figure 13: PMC in compression and extension in the $\boldsymbol{\sigma_1}$-$\boldsymbol{\sigma_3}$ plane

To formulate PMC into the p-q plane equation (48) is expanded and rearranged:

$$(\sigma_I - \sigma_{III}) = (\sigma_I + \sigma_{III})sin\phi_{c,e} + 2c_{c,e}cos\phi_{c,e} \tag{49}$$

During conventional triaxial compression the stress state is $\sigma_I = \sigma_a$ and $\sigma_{II} = \sigma_{III} = \sigma_r$ and equation (49) becomes:

$$(\sigma_a - \sigma_r) = (\sigma_a + \sigma_r)sin\phi_c + 2c_c cos\phi_c \tag{50}$$

Rearranging equation (50):

$$(\sigma_a - \sigma_r)\left(3 - sin\phi_c\right) = 2(\sigma_a + 2\sigma_r)sin\phi_c + 6c_c cos\phi_c \tag{51}$$

To express PMC in terms of the stress invariants p and q, equations (6) and (7) can be substituted into equation (51):

$$q\left(3 - sin\phi_c\right) = 6psin\phi_c + 6c_c cos\phi_c \tag{52}$$

Rearranging it becomes:

$$q = \frac{6sin\phi_c}{3 - sin\phi_c}p + \frac{6c_c cos\phi_c}{3 - sin\phi_c} \tag{53}$$

Using the same approach, an equation for the conventional triaxial extension condition can be written:

$$q = -\frac{6sin\phi_e}{3+sin\phi_e}p - \frac{6c_e cos\phi_e}{3+sin\phi_e} \tag{54}$$

To satisfy the requirement of all planes intersecting at V_0, the following fitting procedure was developed. Figure 14 shows a sketch in p-q plane of the PMC failure criterion with the extension line moved to the compression side of the p-axis. It will be convenient later for the sign convention of θ in the π-plane (Fig. 15) to move the extension line. Knowing the compression and extension line intersect the q-axis at b_c and b_e respectively, the slopes can be written:

$$m_c = \frac{b_c}{V_0}, m_e = \frac{b_e}{V_0} \tag{55}$$

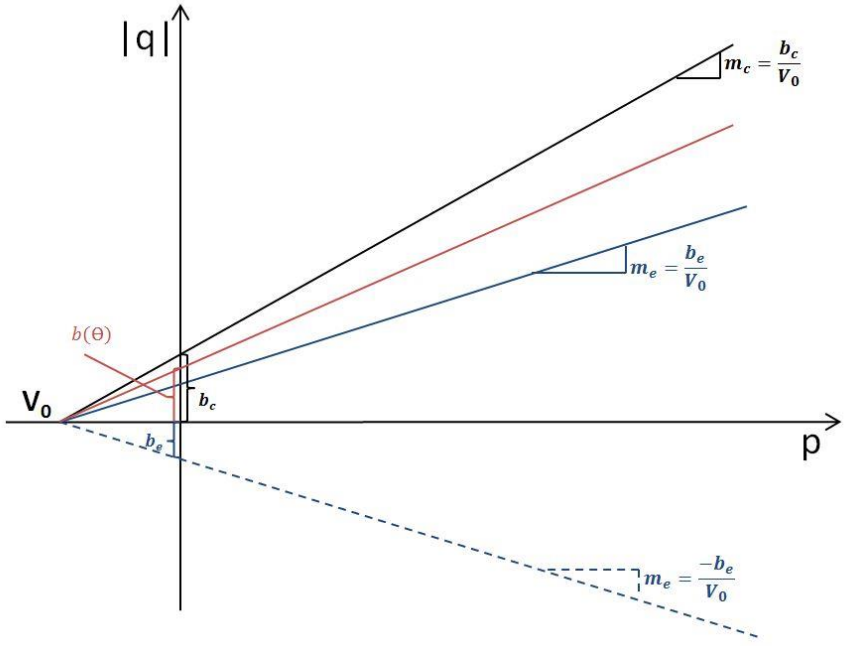

Figure 14: Sketch of the extension line moved to the positive side of p-axis

Using the general equation for a line in p-q plane (25), and the slopes defined in equation (55), the PMC failure criterion can be written for compression as:

$$q_c = \frac{b_c}{V_0} p + b_c = b_c \left(\frac{p}{V_0} + 1 \right) \tag{56}$$

And for extension as:

$$q_e = \frac{b_e}{V_0} p + b_e = b_e \left(\frac{p}{V_0} + 1 \right) \tag{57}$$

A line that intersects the p-axis at V_0 and the q-axis between b_c and b_e (i.e. $b_c \geq b \geq b_e$) can be written as:

$$q = b \left(\frac{p}{V_0} + 1 \right) \tag{58}$$

The intercept b can be in terms of θ in the π-plane (Fig. 15). When θ = 0° this is the condition for a conventional triaxial compression state of stress because $\sigma_2 = \sigma_3$. When θ = 60° this condition represents conventional triaxial extension because $\sigma_1 = \sigma_2$. Equation (58) can be rewritten:

$$q = b(\theta) \left(\frac{p}{V_0} + 1 \right) \tag{59}$$

where $b_c = b(0°) \geq b(\Theta) \geq b_e = b(60°)$

Now the intercept b(θ) must be defined. To do this, a relationship is built between r in the π-plane and q. A line in the π-plane can be written in polar coordinates (Fig. 15):

$$r\cos(\Theta) = k * r\sin(\Theta) + r_c \tag{60}$$

where k is the slope of the line in the π-plane (fig. 15)

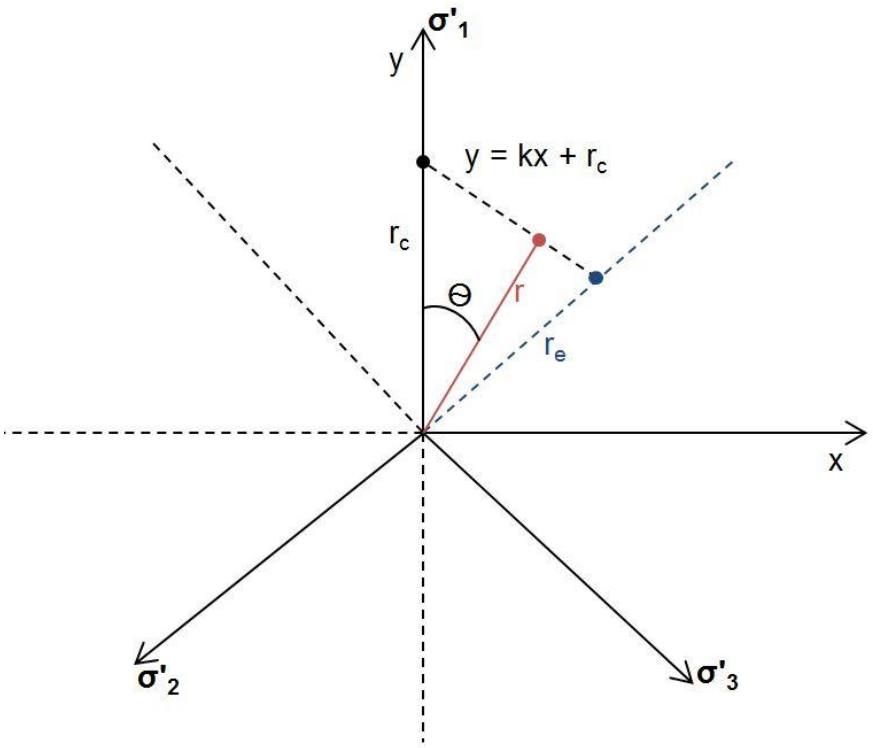

Figure 15: Sketch of linear failure criteria in the π-plane

Equation (60) is solved for r, the distant from the hydrostatic axis to any point on the failure surface in the π-plane:

$$r = \frac{r_c}{\cos(\Theta) - k\sin(\Theta)} \tag{61}$$

It has been shown that the distance r in principal stress space can be related to q $\left(r = \sqrt{\frac{2}{3}}q\right)$ through the use of the second stress invariant J_2 (Davis and Selvadurai 2002). Using this relationship, equation (61) can be written in terms of q:

$$\sqrt{\frac{2}{3}}q = \frac{\sqrt{\frac{2}{3}}q_c}{\cos(\Theta) - k\sin(\Theta)} \tag{62}$$

$$q = \frac{q_c}{\cos(\Theta) - k\sin(\Theta)} \tag{63}$$

Using equations (56) and (59) in (63) and simplifying, a formula for $b(\Theta)$ can be obtained:

$$b(\Theta) = \frac{b_c}{\cos(\Theta) - \mathrm{k}\sin(\Theta)} \tag{64}$$

Equation (64) represents an equation for the intercept b in the p-q plane that depends on θ in the π-plane. Equation (64) contains an unknown variable k representing the slope of a line in the π-plane. To determine this variable, $\Theta = 60^o$ is used in equation (60) to represent a conventional triaxial extension stress state ($r = r_e$):

$$r_e = k\sqrt{3}r_e + 2r_c \tag{65}$$

Equation (65) can be solved for the slope k:

$$k = \frac{1 - 2\frac{r_c}{r_e}}{\sqrt{3}} \tag{66}$$

Using the second stress invariant J_2 to again get a relationship between r and q, the ratio r_c/r_ebecomes:

$$\alpha = r_c/r_e = \sqrt{\frac{2}{3}}q_c \Big/ \sqrt{\frac{2}{3}}q_e \tag{67}$$

The variable k is then rewritten in terms of α:

$$k = \frac{1 - 2\alpha}{\sqrt{3}} \tag{68}$$

Knowing the expression for $b(\Theta)$ and k, equation (59) becomes:

$$q = \frac{b_c}{\cos(\Theta) - \mathrm{k}\sin(\Theta)}\left(\frac{p}{V_0} + 1\right) \tag{69}$$

and can be rewritten as:

$$q\cos(\Theta) = \frac{b_c}{V_0}p + kqsin(\Theta) + b_c \tag{70}$$

Using equation (70), a system of linear equations can be constructed using conventional triaxial compression and extension data. Knowing that for a conventional triaxial compression test $\Theta = 0°$ and for extension $\Theta = 60°$, experimental results can be input into equation (70) and a system of linear equations is created with the form B = Ax, where A is a rectangular m-by-n matrix and B is a vector of m rows.

$$\begin{bmatrix} q_1\cos(\Theta_1) \\ q_2\cos(\Theta_2) \\ \vdots \end{bmatrix} = \begin{bmatrix} Ap_1 & Bq_1\sin(\Theta_1) & C \\ Ap_2 & Bq_2\sin(\Theta_2) & C \\ & \vdots & \end{bmatrix} \tag{71}$$

This problem is solved using MATLAB's backslash command, which returns a least-squares solution to the system of equations. After the constants $A = \frac{b_c}{V_0}$, $B = k$, and $C = b_c$ are determined, the uniform triaxial tensile strength V_0 can be easily solved:

$$V_0 = \frac{b_c}{A} \tag{72}$$

PMC can be constructed in the π-plane using the same method described for MC and HB. By substituting the correct ordering of equations (10-12) into equation (44) will give an equation describing each π-plane failure surface.

Chapter 3: Experimental techniques

An apparatus capable of performing multi-axial testing using two rigid platens and confining pressure was designed and fabricated. This apparatus is a modification of the Plane-Strain Apparatus, U. S. Patent number 5,063,785, developed at the University of Minnesota. The existing device was designed to test rock or concrete having uniaxial compressive strength no greater than 35 MPa. The Plane-Strain Apparatus was capable of continuous monitoring of axial and lateral displacement, axial force, and lateral displacement of the top platen attached to a linear bearing. Setup, instrumentation, and method by which plane-strain condition was achieved have been described (Labuz et al., 1991, 1996). In the design of a true triaxial apparatus, a major goal was to retrofit the existing device such that true triaxial testing was achievable, while maintaining ability to easily convert the device back to plane strain if desired.

3.1 Development

The plane strain apparatus is capable of testing a prismatic rock specimen in a multi-axial setting. However, only the maximum and minimum principal stresses are controllable; the intermediate stress is developed passively through restraint of specimen displacement by a stiff biaxial frame (Labuz et al., 1996). During modification, methods in which the maximum (axial) and minimum (lateral) stresses were applied to the specimen were not altered. Maximum axial stress was applied using a 1 MN servo-hydraulic MTS load frame. Minimum lateral stress was developed through fluid pressure applied inside a large pressure cell. Method of intermediate lateral stress application and control will be modified. The factors that drove the design of this true triaxial apparatus will be discussed. It was decided the best approach to apply stress in the intermediate direction was through hydraulic pistons (Fig. 16). Several important factors guided the piston design and the modification to the plane-strain apparatus.

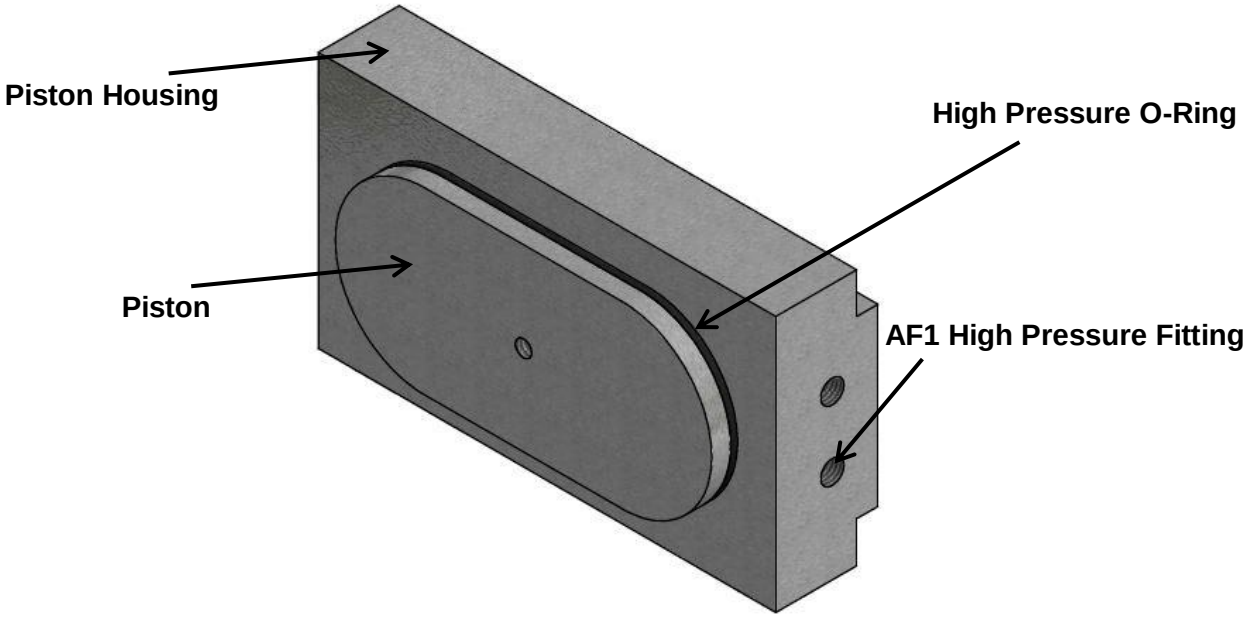

Figure 16: Piston assembly

3.1.1 Piston assembly geometry

There was a restriction on the amount of space available inside the biaxial frame. The inside diameter of the biaxial frame is 110 mm. The existing system of a spacer and wedge occupied approximately 10 mm of the inside diameter, leaving room for a specimen length of 100 mm. It was essential that the design of the new system use minimum space to allow for a maximum specimen length (Fig. 17).

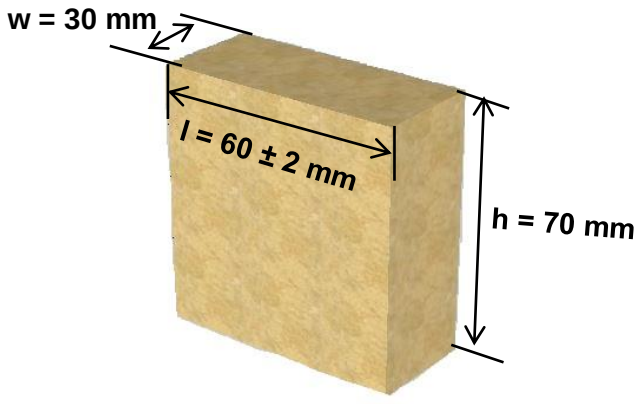

Figure 17: Diagram of specimen dimensions

The piston was designed to leave a maximum available length for the specimen. The piston assembly is composed of two major components, a piston housing and piston (Fig. 16). The versatility of the piston design provided two advantages in terms of space saving. It can be retracted to maximize space for the specimen, and also extended to accommodate specimens of smaller length. Piston assemblies were designed to be a retracted thickness of 23.9 mm and a fully extended thickness of 29.9 mm (Fig. 18).

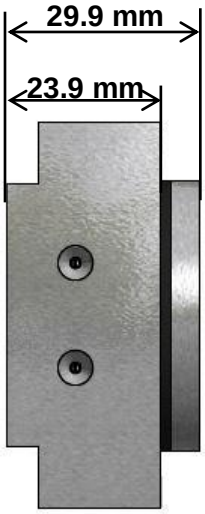

Figure 18: Top view of piston assembly.

A minimum specimen thickness of 30 mm was desired and was a guiding factor in design. On the biaxial frame there are two, diametrically opposed, flat surfaces designed to react against the specimen in the lateral direction (Labuz et al., 1996). These machined surfaces are 41 mm wide and extend the 107 mm height of the biaxial frame. To accommodate a minimum specimen thickness of 30 mm the piston housing needed to be machined as shown in figure 19.

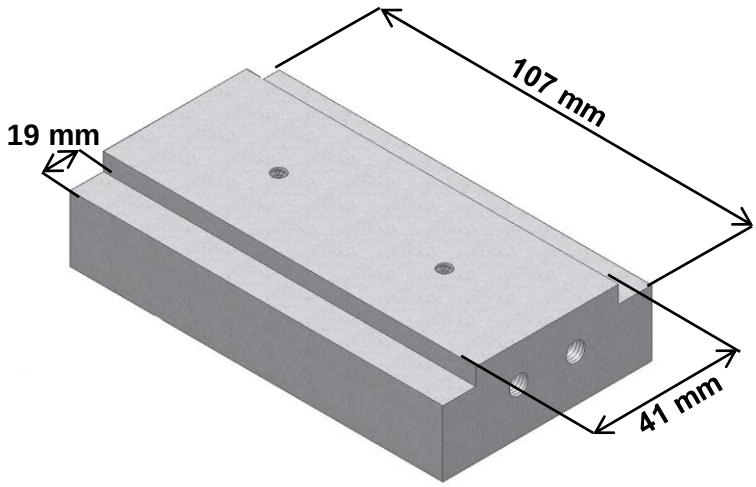

Figure 19: View of housing back showing machining required to accommodate width dimensions

The piston housing back was machined to match the size of the flat surfaces on the biaxial frame. However, to allow for the minimum specimen thickness, the front of the housing needed to be 60 mm. To achieve this, the geometry in figure 13 was used. This design occupied minimal space, attached directly to the existing biaxial frame, and allowed for the minimum desired specimen thickness to be achieved.

3.1.2 Intermediate force capacity

Force capacity in the intermediate direction was another driving factor of piston assembly design. To arrive at a desired force capacity in the intermediate direction, existing capacities of the plane-strain apparatus were considered. The linear bearing on the plane-strain apparatus, through which the maximum axial force is applied, has a capacity of 450 kN (~225 MPa stress on specimen). The pressure vessel allowing for application of the minimum principal stress through pressurization of confining fluid was rated for 24 MPa (Labuz et al., 1996). Using the previous two capacities as reference, a stress capacity in the intermediate direction of 100 MPa was chosen. Knowing the specimen area that intermediate force would be applied over (A_2 = 2100 mm^2), a force of 198 kN would provide the desired stress. Force of the piston assembly is developed through hydraulic

pressure. A microprocessor-based hydraulic pump that could deliver 69 MPa provided the hydraulic pressure to the piston assembly. Force was developed by the hydraulic pressure that acted over the area of the back of the piston:

$$F_p = \sigma_p * A_p \tag{73}$$

where

$F_p = piston\ force$

$\sigma_p = hydraulic\ pressure$

$A_p = area\ of\ piston\ exposed\ to\ hydraulic\ presure$

Changing the piston area would change the force that could be achieved. Satisfying the first two design criteria resulted in a piston area of 2,873.7 mm^2 (Fig. 20). Using the available hydraulic pressure of 69 MPa acting over an area of 2,873.7 mm^2, an estimated piston force of 198.3 kN could be generated. This value satisfied the desired intermediate force capacity.

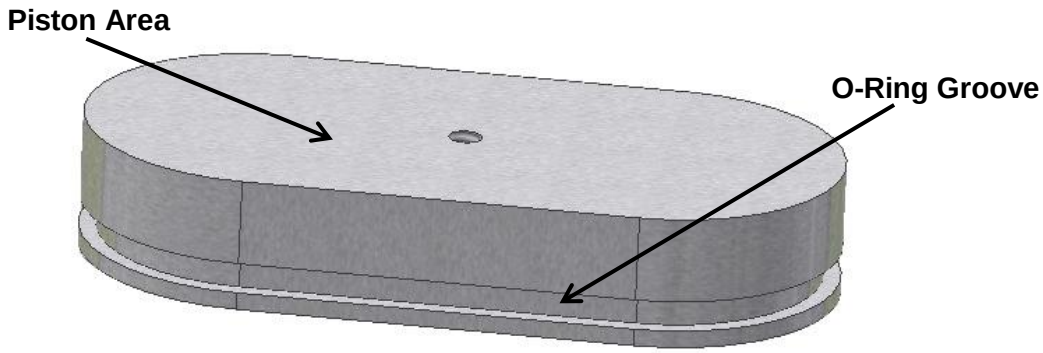

Figure 20: Piston design

3.1.3 Stress analysis

Prior to fabrication, it was important to ensure stresses developed within the piston assembly during maximum hydraulic pressure would not exceed the yield

stress of the housing material. To explore this, a 3D finite element model was used to numerically analyze the piston assembly. Piston housing geometry shown (Fig. 16, 18, and 19) was used for the simulation. For simplicity, the high pressure fittings located on top of the housing were neglected during simulations. Zero displacement was prescribed as the boundary condition for the housing back. All boundaries within the machined portion of housing where the piston is placed were subject to a pressure of 69 MPa. Material parameters from A2 tool steel (E = 207 GPa, v = 0.3 and σ_Y = 250 MPa) were used for piston housing material.

Contours of the maximum shear stress are shown (Fig. 21). The portion of the piston housing subjected to the largest shear stress is the center of the flat machined edge oriented parallel to the length. The shear stress found along that edge was approximately 98 MPa, which was a very safe stress level for A2 tool steel (σ_Y = 250 MPa).

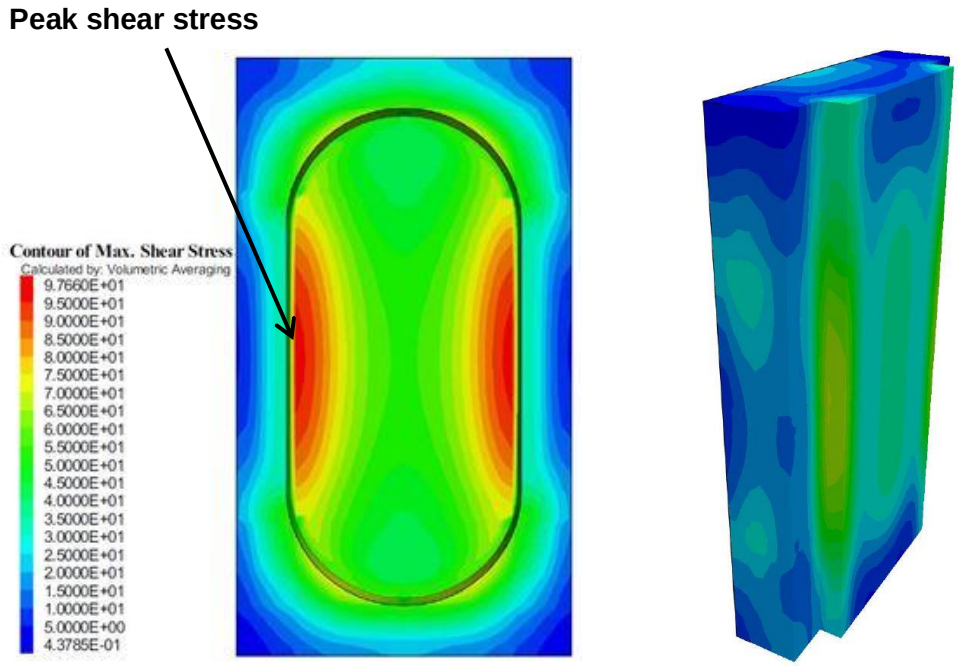

Figure 21: Plane and side view showing maximum shear stress

Displacement of the housing was also modeled (Fig. 22) because deformation was of particular interest. An O-ring placed in the groove shown in figure 20 sealed the interface between the piston and housing. To ensure that the O-ring would seal at that interface a tight tolerance of 0.025 mm was needed between the piston and housing. The piston assemblies were fabricated to meet this tolerance when no hydraulic pressure was being applied. However, when pressure is applied the piston housing will undergo deformation and the tolerance needed for the O-ring to seal could be exceeded. The largest deformation found at the contact between the piston and housing was approximately 0.025 mm. This displacement was not large enough to cause safety concerns, but was sufficiently large to potentially cause leakage at high pressures. This issue was resolved by selecting the proper O-ring.

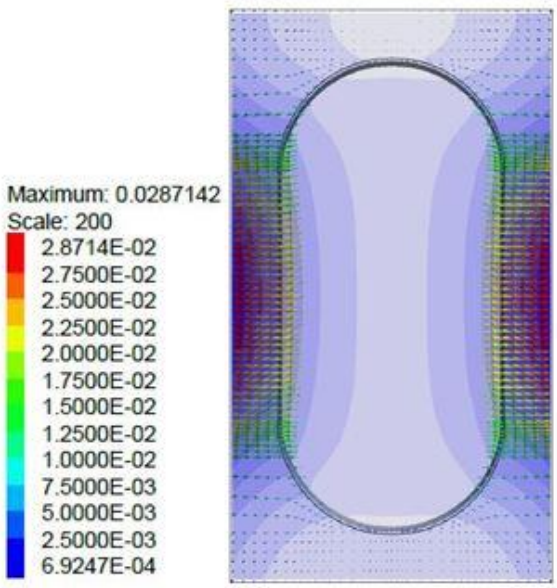

Figure 22: Plane view showing displacement of piston housing

O-rings seal interfaces through a method called squeeze. Squeeze is measured as the percentage an O-ring is deformed when confined between two interfaces. Selecting an O-ring with a larger cross section allowed for more squeeze and therefore accommodation of the displacement of the housing wall during high

hydraulic pressures. A Parker HNBR O-ring with an inside diameter of 60.0 mm and a cross section of 2.61 mm was selected. The specification of squeeze for this O-ring was a minimum of 15.8% and a maximum of 20.8%. Analyzing the squeeze of the O-ring with no hydraulic pressure and with maximum hydraulic pressure resulted in the following. With no pressure in the piston housing, the O-ring would experience 20.6% squeeze and at maximum pressure 19.5% squeeze. This is within the tolerance at both pressure extremes, so leakage was not of concern if the housing undergoes displacement similar to that predicted in the simulation.

In the simulation results, the shear stress found in the piston housing at a hydraulic pressure of 69 MPa was approximately 63% of the yield stress of A2 tool steel. Although no failure concerns were found using parameters of A2 steel a larger factor of safety was desired, so higher strength steel was chosen. Steel 4340, a nickel-chromium-molybdenum alloy steel with E = 205 GPa and σ_Y = 710 MPa was chosen. Through the use of steel 4340 the maximum predicted stresses at peak hydraulic pressure decrease to 22% of the yield stress. This greatly increased the safety factor, and ensured that if pressures greater than 69 MPa are desired in the future the strength of the housing will not be a limiting factor.

3.1.4 Calibration

After the piston assemblies were fabricated and placed within the plane-strain apparatus, calibration was necessary to investigate the force that was being applied to the specimen in the intermediate direction. The force generated by the piston assemblies was governed by equation (45). However, the force being transferred to the specimen at a given hydraulic pressure was reduced once confining pressure was applied. This was because the piston assemblies were submerged in confining fluid and thus exposed to confining pressure (Fig. 23). The reduction in force applied to the specimen was the exposed piston area ($A_p - A_2$) multiplied by the confining pressure (σ_3).

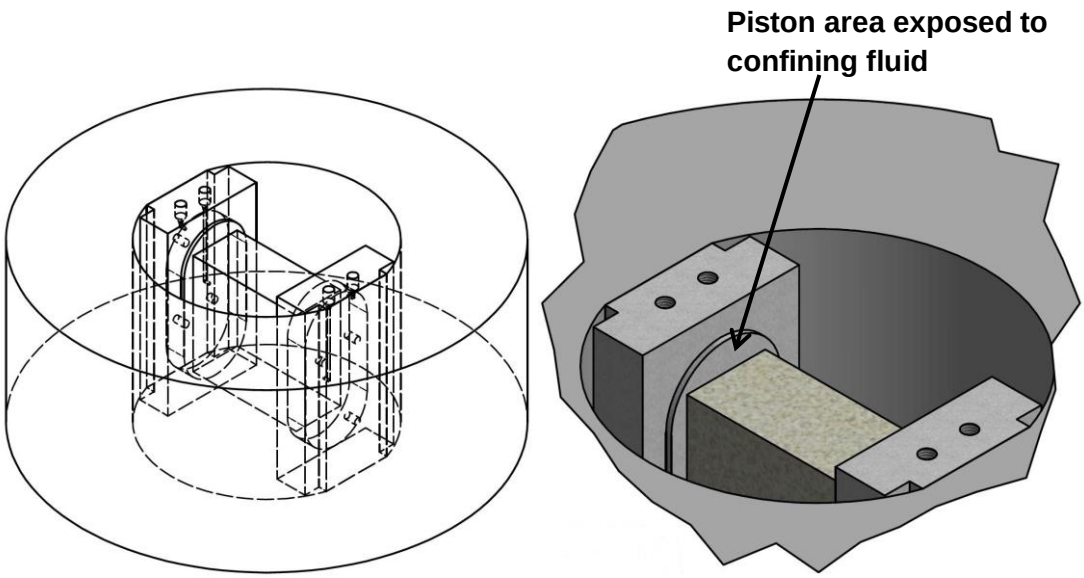

Figure 23: Sketch of specimen in place in biaxial frame

To calibrate the piston assemblies, several loading and unloading sequences in the intermediate direction were performed at various confining pressures. These sequences were performed using an instrumented aluminum 6061 specimen. The aluminum specimen has a length of 68 mm, height of 70 mm, and thickness of 30 mm. The specimen was instrumented with one micro-measurements EA-00-250TM-120 biaxial strain rosette. The gage was installed on the 68 x 70 mm face and measured strain in the axial and intermediate direction (ε_1 and ε_2). The experiment was performed as follows.

First, an axial stress (σ_1) of 75 MPa was applied to the specimen. Axial stress remained constant and was the maximum principal stress in magnitude throughout the testing. Next, confining pressure (σ_3) was applied such that a condition $0 \leq \sigma_3 \leq 20\ MPa$ was satisfied. Confining pressure remained constant during each intermediate stress loading sequence. Normal stress was then applied to the specimen in the intermediate (σ_2) direction by the piston assemblies, while ensuring the condition of $\sigma_3 < \sigma_2 < \sigma_1$ was always satisfied.

The force applied to the specimen was calculated using the following equation:

$$F_p = \sigma_p A_p - \sigma_3 (A_p - A_2) \tag{74}$$

where

$\sigma_3 = confining\ pressure$

$A_2 = specimen\ area\ contacting\ the\ piston\ in\ intermediate\ direction$

Using the force calculated from equation (74), the stress developed in the specimen in the intermediate direction is simply:

$$\sigma_2 = \frac{F_p}{A_2} \tag{75}$$

where σ_2 is stress on specimen in the intermediate direction

To relate intermediate stress to intermediate strain, incremental Hooke's Law was used:

$$\Delta\varepsilon_2 = \frac{\Delta\sigma_2}{E} - \frac{\nu}{E}(\Delta\sigma_1 + \Delta\sigma_3) \tag{76}$$

where

$\Delta\varepsilon_2 = change\ in\ intermediate\ strain$

$\Delta\sigma_1 = change\ in\ major\ principal\ stress\ (axial\ stress)$

$\Delta\sigma_2 = change\ in\ intermedeate\ principal\ stress$

$\Delta\sigma_3 = change\ in\ minor\ pricipal\ stress\ (confining\ stress)$

$E = Young's\ Modulus$

During testing, the axial and confining stresses remained constant, so equation (76) is simplified to:

$$\Delta\varepsilon_2 = \frac{\Delta\sigma_2}{E} \tag{77}$$

Substituting equations (74) and (75) into equation (77) Hooke's Law can be rewritten as:

$$\Delta\varepsilon_2 = \frac{\left(\Delta\sigma_p A_p - \sigma_3\left(A_p - A_2\right)\right)/A_2}{E} \tag{78}$$

Solving equation (78) for piston area (A_p) gives:

$$A_p = \frac{A_2(\Delta\varepsilon_2 E - \sigma_3)}{\Delta\sigma_p - \sigma_3} = \frac{\beta}{\alpha} \tag{79}$$

Equation (79) was used to determine the correct position area over which hydraulic pressure was acting. All terms in equation (79) were either directly measured or known material parameters. Calibration tests were performed at $\sigma_3 = 0, 5, 10, 15, and\ 20\ MPa$ and all are shown in (Fig. 24) excluding $\sigma_3 = 0\ MPa$. Fitting a trend line to the tests gives an A_p = 2870.9 mm^2.

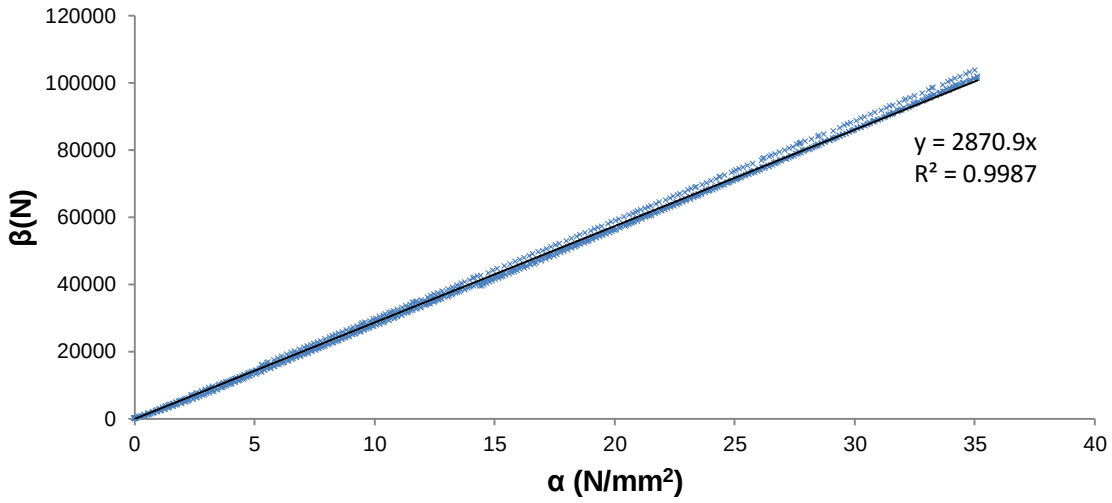

Figure 24: Piston area calibration for $\boldsymbol{\sigma_3 = 5, 10, 15, and\ 20\ MPa}$

As with any measuring device, there is a tolerance associated with the reading. Table 1 shows the areas obtained from each calibration test and the tolerance of the measurement. The piston area obtained from the average of calibration tests performed at $\sigma_3 = 5, 10, 15, and\ 20\ MPa$ is 0.1% smaller than the piston area

calculated from the piston geometry. The cause of this was attributed to the complex way the confining pressure and hydraulic pressure interact within the O-ring groove.

Table 1: Piston area obtained for each value of σ_3

σ_3 (MPa)	A_p (mm^2)	R^2	± (%)
0	2838.2	0.998	2.0
5	2944.4	0.996	2.0
10	2992.1	0.999	1.5
15	2897.0	0.999	2.0
20	2884.6	0.999	1.5

3.1.5 Constant mean stress testing

It is convenient for performing analysis in principal stress space to conduct true triaxial experiments under constant mean stress. During constant mean stress testing, the mean the stress at the beginning of testing, throughout loading/unloading, and at failure are equal ($p_i = p_f = p$). An experimental method was developed such that constant mean stress testing was achievable ($\Delta p = 0$). Change in mean stress was written in terms of three principal stresses:

$$\Delta p = \frac{\Delta\sigma_1 + \Delta\sigma_2 + \Delta\sigma_3}{3} \tag{80}$$

Experimentally maintaining a condition of $\Delta p = 0$, while simultaneously changing all three principal stresses is challenging. Equation (80) can be simplified by holding one principal stress constant ($\Delta\sigma_3 = 0$):

$$\Delta p = \frac{\Delta\sigma_1 + \Delta\sigma_2}{3} \tag{81}$$

Knowing for constant mean stress $\Delta p = 0$ equation (81) becomes:

$$\Delta\sigma_1 = -\Delta\sigma_2 \tag{82}$$

To satisfy equation (82), if $\Delta\sigma_1$ and $\Delta\sigma_2$ are increased and decreased at the same ratio constant mean stress will be maintained. Calibration experiments were performed using an instrumented aluminum 6061 specimen with known elastic parameters. Calibration was performed using $\sigma_3 = 0\ MPa$ and at $t = 0\ sec$ $\sigma_1 = \sigma_2 = 40\ MPa$ giving a mean stress $p = 26.7\ MPa$. Target mean stress was maintained within ± 0.1 MPa (Fig. 25).

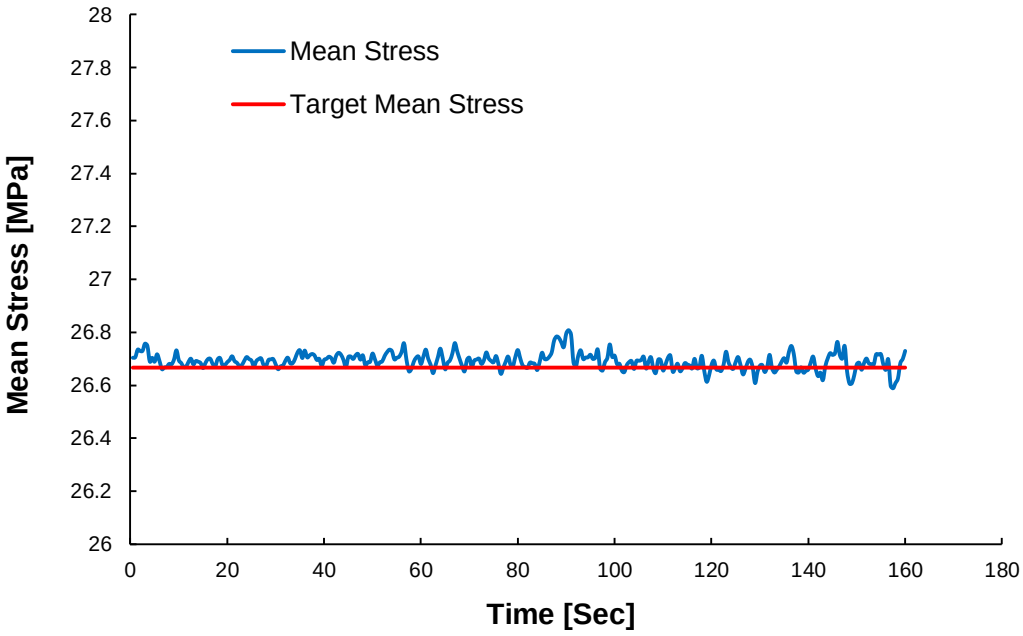

Figure 25: Mean stress achieved vs. target mean stress

3.2 Petrographic analysis

Dunnville sandstone was selected for experimentation because of desirable strength properties and readiness. Petrographic analysis was performed and the sandstone was classified as a fine to medium-grained quartz arenite. Mineral composition was more than 90% quartz with little to no cement matrix. Full mineralogy of the Dunnville sandstone is found in Table 2. Rock was highly porous with a porosity of 29-30%. Sandstone was bedded with “lighter” and “darker” beds differentiated primarily by their average grain size and sorting. Darker beds were primarily fine to medium-grained (0.05 mm to 0.25 mm) poorly

sorted quartz and feldspar grains. Lighter beds were primarily fine-grained (0.05 mm to 0.125 mm) well sorted quartz and feldspar grains. Elongate biotite crystals were present in both beds and were oriented subparallel to bedding.

Table 2: Mineralogy of Dunnville sandstone

Mineral	Vol (%)
Quartz	90 - 95
Alkali Feldspar	2 - 5
Plagioclase	trace-1
Biotite	2 - 5
Muscovite	trace
Clinozoisite	trace
Zircon	trace
Hematite	trace
Iron-Oxide	1 - 2

Thin sections impregnated with fluorescent dye were analyzed under plane polarized transmitted light are shown in (Fig. 26). Quartz crystals are shown in white and pore space in yellow. Elongate brown crystals oriented sub parallel to one another are mica (biotite, muscovite, and clinozoisite) flakes. Mica flakes shows strong subparallel orientation with bedding.

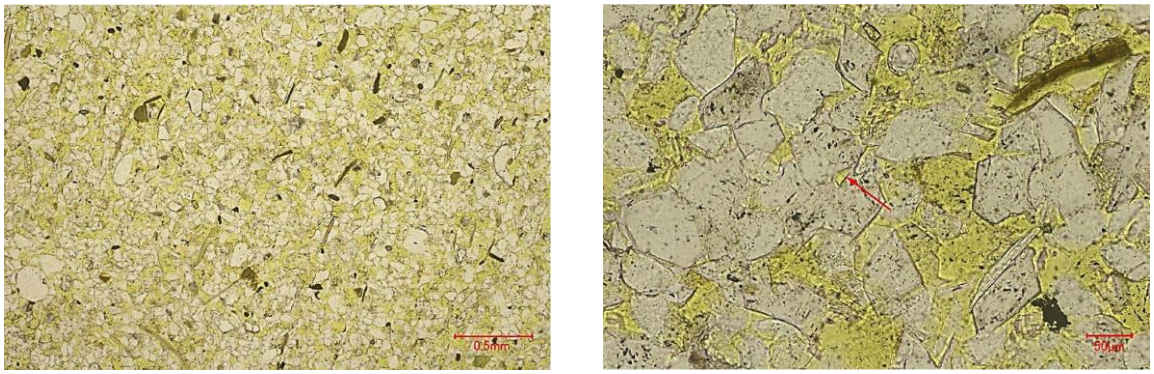

Figure 26: Thin section under plane polarized light (Left image 40x Right image 200x)

3.3 Specimen preparation

Uniaxial, conventional, and true-triaxial specimens were prepared from a single 30.5cm (12 in.) x 30.5cm (12 in.) x 30.5cm (12 in.) block of Dunnville sandstone. Uniaxial specimen dimensions were a diameter of 50.0 ±1.0 mm and length 100 ±2.0 mm. Conventional triaxial specimen dimensions were a diameter of 30.5 ±0.5mm and length 80 ±2.0mm. Dimensions for true-triaxial specimens were 61 ±1.0mm x 69 ±1.0mm x 30 ±0.5mm. A table saw with a 30.5cm (12 in.) diamond saw blade was used to wet cut specimens to approximate final dimensions. Specimens were then wet ground using a surface grinder with an aluminum oxide grinding wheel. Conventional triaxial specimen ends were machined flat to within 0.02mm and did not depart from perpendicularity to longitudinal axis by more than ±0.05mm. True-triaxial specimen surfaces were machined parallel to the opposite face and orthogonal to the adjacent faces. Conventional triaxial specimens were prepared with length oriented perpendicular to bedding; true-triaxial specimens were prepared with height oriented perpendicular to bedding (Fig. 27). All specimens were placed in an oven at 70°C to dry for 24 hours prior to testing.

Figure 27: Prepared conventional and true-triaxial specimens.

3.4 Conventional triaxial testing

Conventional triaxial testing was performed using a Hoek-Franklin pressure cell. The Hoek-Franklin cell allows for the independent application of axial (σ_a) and radial stresses (σ_r). The cell was designed for specimens of diameter 31.0mm and length approximately 80mm. Radial stress was developed through fluid pressure provided by a microprocessor controlled hydraulic screw-type intensifier. Fluid pressure was increased or decreased by advancing or retracting the intensifier through the use of an electric stepper motor. Axial stress was developed through a 1 MN MTS servo-hydraulic load frame. Instrumentation connected to a data acquisition system recorded axial force, axial displacement, and confining stress.

A unique feature of the Hoek-Franklin triaxial cell is the one-piece synthetic rubber membrane used to prevent hydraulic oil from contacting the specimen. The membrane ends are specially designed to allow for the application of confining pressure (≤ 69 MPa) without leakage. The inside surface of the membrane, which contacted the specimen, was coated with stearic acid to reduce frictional affects from the membrane and also assist with the insertion and removal of specimens (Labuz & Bridell, 1993).

A conventional triaxial compression stress path involved increasing axial ($\sigma_1 = \sigma_a$) and radial stress ($\sigma_r = \sigma_2 = \sigma_3$) hydrostatically to a desired mean stress value. Specimens were brought to failure through axial loading (increase of mean stress and deviator stress) by specification of a closed-loop, computer controlled axial displacement rate of 2 x 10^{-3} mm/s ($\Delta\sigma_a > 0$ and $\Delta\sigma_r = 0$).

A conventional triaxial extension stress path involved increasing axial ($\sigma_3 = \sigma_a$) and radial stress ($\sigma_r = \sigma_1 = \sigma_2$) hydrostatically to a desired mean stress value. Specimens were brought to failure through axial unloading (decrease in mean stress and absolute value increase in deviator stress) by specification of axial displacement rate of 0.5 x 10^{-3} mm/s ($\Delta\sigma_a < 0$ and $\Delta\sigma_r = 0$).

3.5 True-triaxial constant mean stress testing

Constant mean stress tests were performed using the apparatus discussed previously. Prior to testing, specimens were coated with polyurethane to prevent confining fluid from contacting the specimen (Fig. 28). Brass buttons were adhered to the front and back of the specimens at the contact locations of the lateral LVDTs. Along with sealing the specimen, polyurethane also aided in assembly by holding the side plates, upper, and lower platens in place.

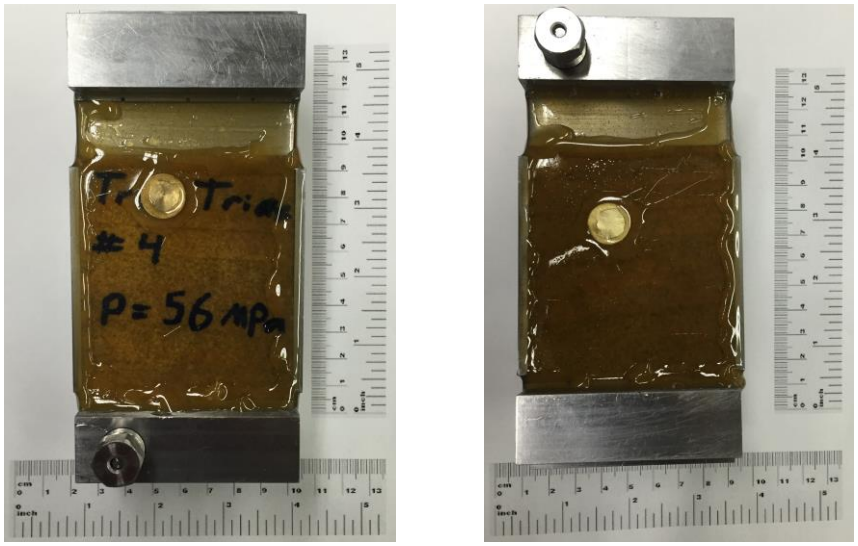

Figure 28: Constant mean stress specimen. Right (front view) Left (back view)

Constant mean stress experiments were performed using a stress path with three loading stages. Stage one began by increasing axial stress (σ_1), intermediate lateral stress (σ_2), and minor lateral stress (σ_3) near hydrostatically until a desired σ_3 was reached. To achieve this, axial stress was increased by specification of an axial displacement rate of 5 x 10^{-4} mm/s. At this small displacement rate, it was easy to monitor $\Delta\sigma_1$ and manually increase $\Delta\sigma_2$ and $\Delta\sigma_3$ at the same rate, maintaining a near hydrostatic condition. The described process was continued until a chosen minor lateral stress level was reached, where σ_3 remained constant. During stage two, σ_1 and σ_2 were increased at the same rate ($\Delta\sigma_1 = \Delta\sigma_2$) until the chosen level of mean stress was reached. Similar

to stage one, axial displacement was increased at a rate of 5 x 10^{-4} mm/s. Intermediate stress was increased at the same rate by advancing the intensifier controlling the hydraulic pressure inside the piston assemblies. At stage three, the specimen was brought to failure by increasing axial stress ($\Delta\sigma_1 > 0$) and decreasing intermediate lateral stress ($\Delta\sigma_2 < 0$) at the same rate ($\Delta\sigma_1 = -\Delta\sigma_2$). Axial stress was increased by specification of an axial displacement rate of 1.0 x 10^{-3} mm/s. Intermediate stress was decreased by retracting the hydraulic intensifier.

Chapter 4: Results and discussion

4.1 Material strength and elastic properties

Uniaxial compression tests were performed on two prismatic specimens with different bedding orientations. One specimen had length oriented perpendicular to bedding and the other was parallel. Evaluating anisotropy was not of primary interest, however due to presence of bedding the degree of anisotropy was investigated. Specimens were instrumented with Micro-Measurements resistive strain gages. The specimens were prepared in accordance with ASTM standards and stressed with a closed-loop servo hydraulic 1 MN MTS load frame. Tests were carried out with an axial displacement rate of 1 x 10^{-3} mm/s. A data acquisition system recorded axial force, axial displacement, and axial and lateral strain at a frequency of 1 Hz. USC and elastic parameters were determined for both bedding orientations. Uniaxial compressive strength is simply:

$$C_0 = \frac{F_{max}}{A} \tag{83}$$

where

$A = cross\ sectional\ area$

Elastic parameters Young's modulus (E) and Poisson's ratio (v) were calculated from axial and transverse strain measurements:

$$E = \frac{\Delta\sigma_a}{\Delta\varepsilon_a} \tag{84}$$

$$\nu = -\frac{\Delta\varepsilon_t}{\Delta\varepsilon_a} \tag{85}$$

where

$\Delta\sigma_a = change\ in\ axial\ stress$

$\Delta\varepsilon_a = change\ in\ axial\ strain$

$\Delta\varepsilon_t = change\ in\ transverse\ strain$

For determination of elastic parameters specimens were loaded to approximately 50% of the uniaxial compressive strength. Figure 29 shows the axial stress - strain response for both specimen orientations with dashed portion indicating elastic region over which Young's modulus was calculated.

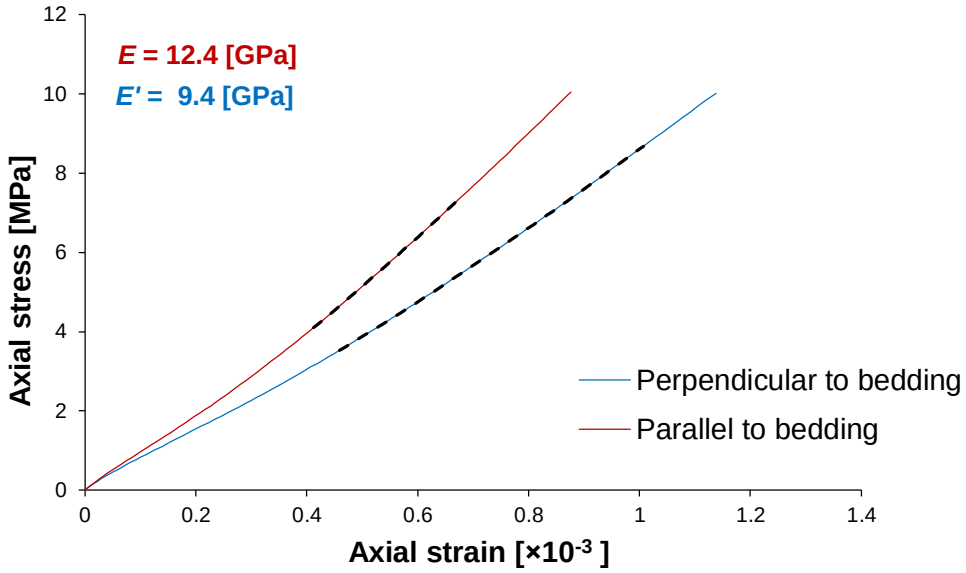

Figure 29: Axial stress vs axial strain

Figure 30 shows the radial - axial strain response. Dashed portion indicates elastic region used to calculate Poisson's ratio. Dashed portion in both figures 29 and 30 represent the same range of axial stress. Perpendicular to bedding, as opposed to parallel to bedding, Young's modulus was 24% higher and Poisson's ratio was 6% higher. Peak axial stress for the two tests was 29.7 and 24.9 MPa for perpendicular and parallel respectively, giving a 16% larger uniaxial compressive strength perpendicular to bedding.

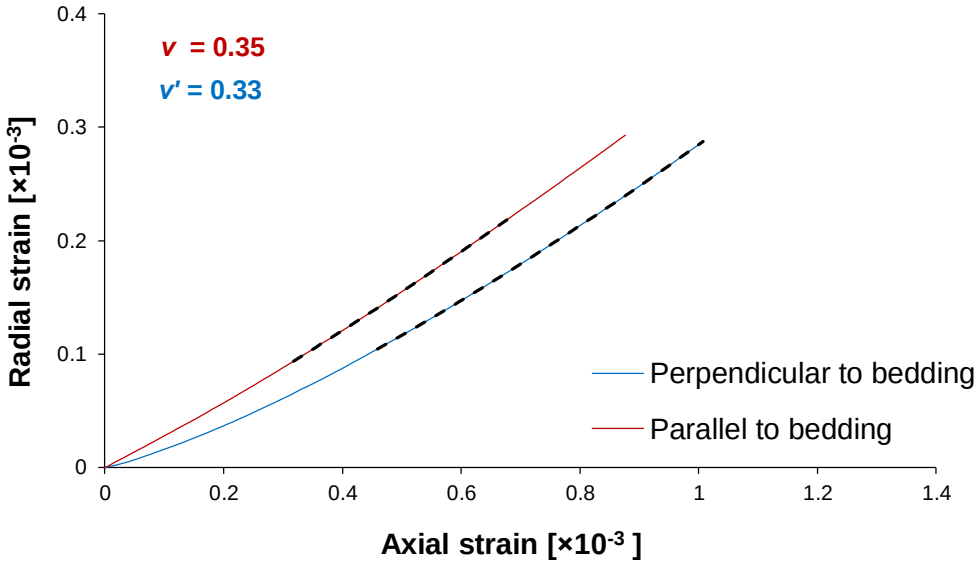

Figure 30: Radial vs axial strain

Thirteen conventional triaxial tests and five multi-axial tests (TT) were performed. Of the twelve conventional triaxial tests, seven were performed in compression (C) and five in extension (E). The principal stresses, mean stress, and deviator stress at failure are shown in table 2. The data in Table 3 will be used in the analysis of the three failure criteria introduced in chapter 2.

Table 3: Conventional triaxial compression-extension results

Stress path	σ_1 (MPa)	σ_2 (MPa)	σ_3 (MPa)	*p (MPa)*	*q (MPa)*
C	29.7	0.0	0.0	9.9	29.7
C	39.4	2.5	2.5	14.8	36.9
C	52.9	5.0	5.0	21.0	47.9
C	71.5	10.0	10.0	30.5	61.5
C	98.4	20.0	20.0	46.1	78.4
C	114.5	30.0	30.0	58.2	84.5
C	129.4	40.0	40.0	69.8	89.4
E	35.0	35.0	0.8	23.6	34.2
E	40.0	40.0	1.2	27.1	38.8
E	50.0	50.0	6.0	35.3	44.0
E	60.0	60.0	10.1	43.4	49.9
E	69.0	69.0	11.5	49.8	57.5
TT	48.3	31.6	5.0	28.3	37.8
TT	53.0	25.1	7.0	28.3	40.1
TT	63.9	12.1	9.0	28.3	53.4
TT	77.5	70.5	20.0	56.0	54.3
TT	83.5	60.5	24.0	56.0	51.9

A distinct failure plane developed in all true-triaxial tests, except one at σ_3 = 5 MPa and p = 28.3 MPa, where the failure plane was a hybrid involving axial splitting and a shear band. The orientation of the failure plane was measured for each of the five tests performed (Fig. 31) and the values are reported in Table 4. The failure plane angle θ shows a dependence on mean stress, with the average orientation θ_{avg} = 73.8° at p = 28.3 MPa and θ_{avg} = 61.5° at p = 56.0 MPa.

Figure 31: True-triaxial specimens. Top: p = 28.3 MPa. Bottom: p = 56 MPa

Table 4: True-triaxial shear fracture angle

Specimen #	σ_1	σ_2	σ_3	p	θ
	[MPa]	[MPa]	[MPa]	[MPa]	[Deg]
1	48.3	31.6	5.0	28.3	73.4
2	53.0	25.1	7.0	28.4	72.9
3	63.9	12.1	9.0	28.3	75.0
4	77.5	70.5	20.0	56.0	62.7
5	83.5	60.5	24.0	56.0	60.3

4.2 Multi-axial stress path

The stress paths during stage two and three loading for tests performed at mean stresses of p = 28.3 and 56.0 MPa are shown (Fig. 32-33). Figure 32 shows the stress vs. axial strain response of all three principal stresses for a test performed at a target mean stress of 28.3 MPa and a constant σ_3 = 9 MPa. The plot begins at the start of stage two loading, stage one loading is hydrostatic and data acquisition was not running during this stage of testing. Response of the specimen during the stage two loading ramp is linear, which suggests in the

stress path shown leading to p = 28.3 MPa the specimen was within a linear elastic region. The left dashed vertical line represents the beginning of stage three loading. During stage three loading mean stress is held constant at to p = 28.3 MPa. At failure, the right dashed line, axial stress decreases rapidly indicating brittle failure.

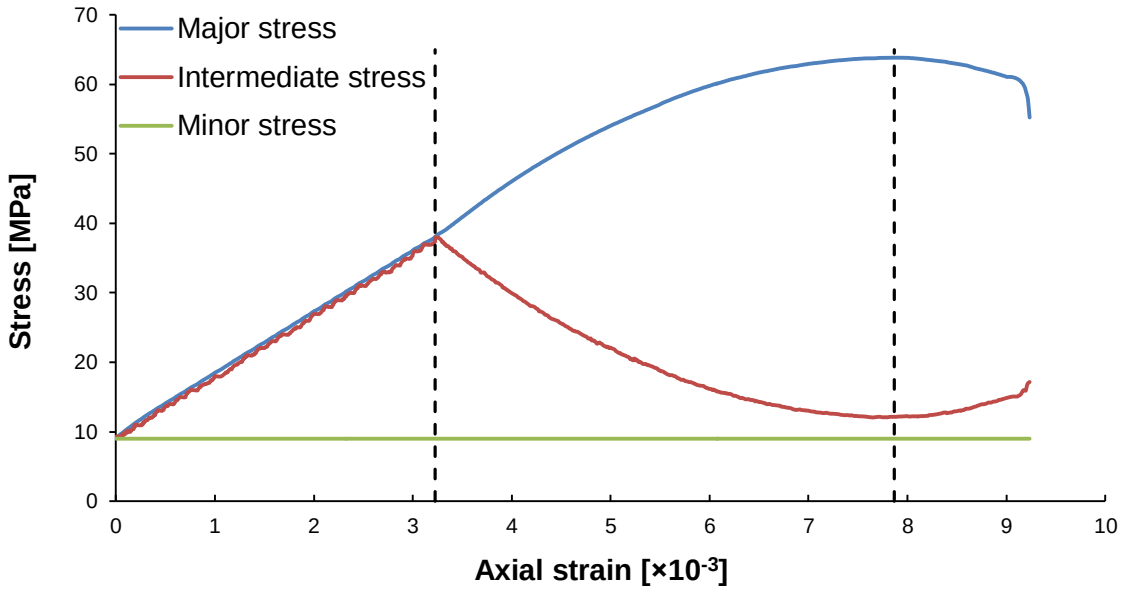

Figure 32: Stress path during stage two and three loading (σ_3 = 9 MPa, p = 28.3 MPa)

Figure 33 shows the stress - axial strain response of all three principal stresses at p = 56.0 MPa and a constant σ_3 = 24 MPa. Again, hydrostatic stage one loading is not shown. During stage two loading the specimen appears to reach a nonlinear region suggesting inelastic deformation was taking place. After peak stress, the specimen behaves in a more ductile matter as is displayed by the small drop in stress at failure followed by a gradual decrease in major stress.

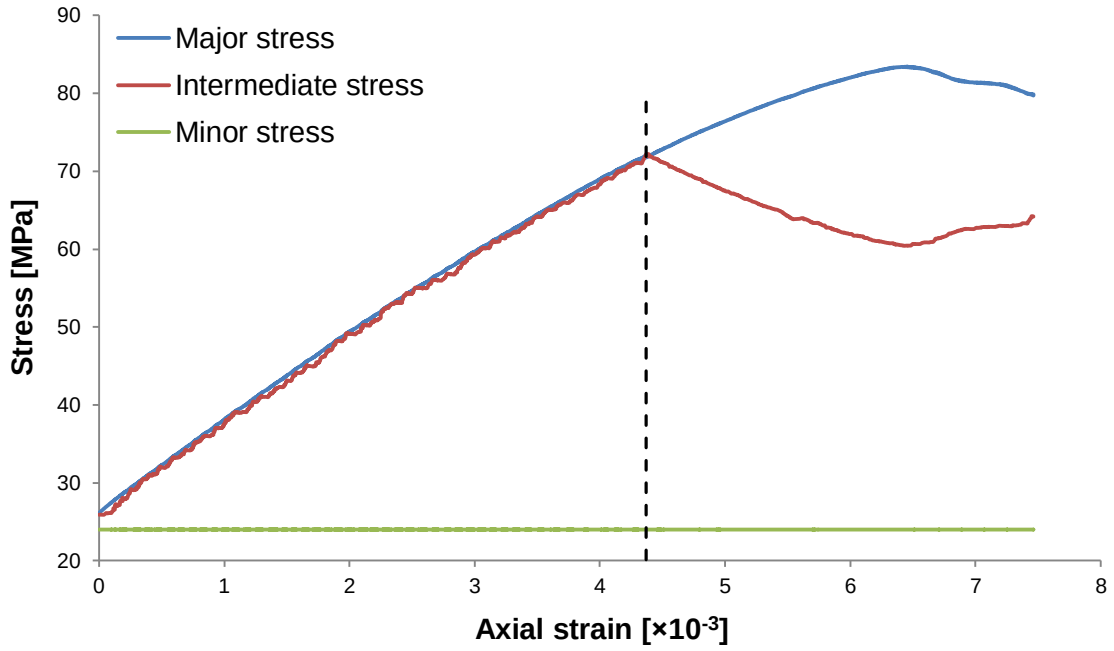

Figure 33: Stress path during stage two and three loading ($\boldsymbol{\sigma_3}$ = 24 MPa, p = 56 MPa)

4.3 Principal plane fitting

The MC criterion was fitted to conventional compression and extension data in the σ_1-σ_3 plane (Fig. 34). To obtain the slope K_p, the MC criterion given in equation (14) was used to fit a line to the compression only. The strength parameters ϕ, c, and V_0 were then calculated:

$$\phi = \sin^{-1}\left(\frac{K_p - 1}{K_p + 1}\right) = \sin^{-1}\left(\frac{2.79 - 1}{2.79 + 1}\right) = \mathbf{28.2°}$$

$$c = \frac{C_0(1 - \sin\phi)}{2\cos\phi} = \frac{29.7(1 - \sin(28.2))}{2\cos(28.2)} = \boldsymbol{8.9\ MPa}$$

$$V_0 = \frac{C_0}{K_p - 1} = \frac{29.7}{2.79 - 1} = \boldsymbol{16.6\ MPa}$$

Knowing the strength parameters, equation (16) was used to plot the MC failure line in extension. The MC criterion is shown to be symmetric about the dashed line ($\sigma_1 = \sigma_3$).

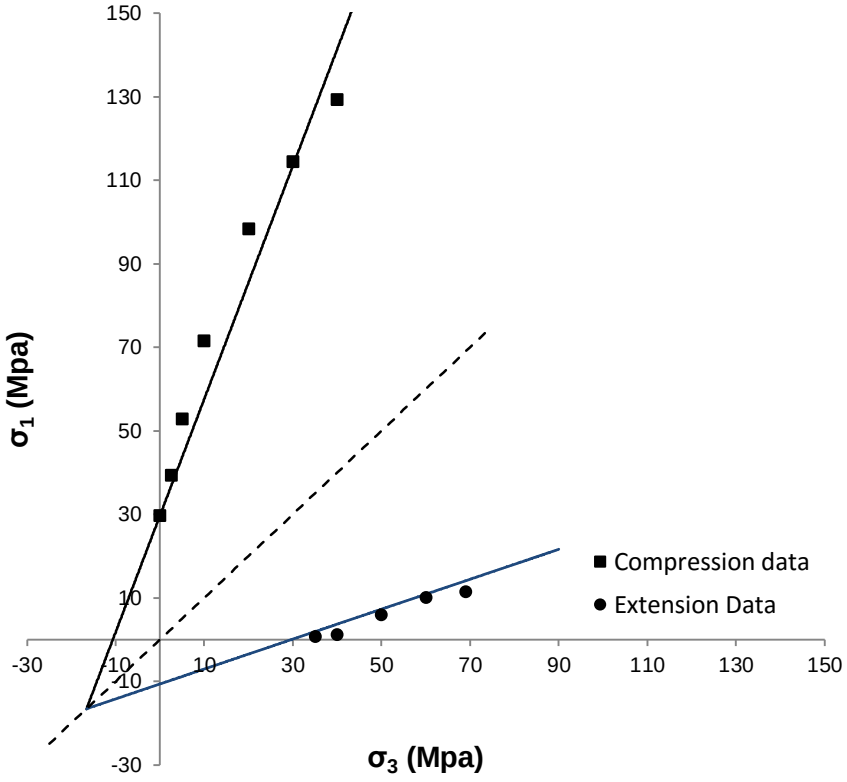

Figure 34: MC σ_1-σ_3 fitting

The HB criterion is plotted in σ_1-σ_3 plane (Fig. 35). To obtain the fitting parameter *m* equation (27) was used to fit the HB criterion to the compression data. A value of m = 7.5 was used for this parameter. Equation (29) was then used to plot the HB extension curve. Knowing the fitting parameter *m*, the strength parameter V_0 was calculated:

$$V_0 = \frac{C_0}{m} = \frac{29.7}{7.5} = \mathbf{3.96\ MPa}$$

HB is shown to be symmetric about the dashed line ($\sigma_1 = \sigma_3$).

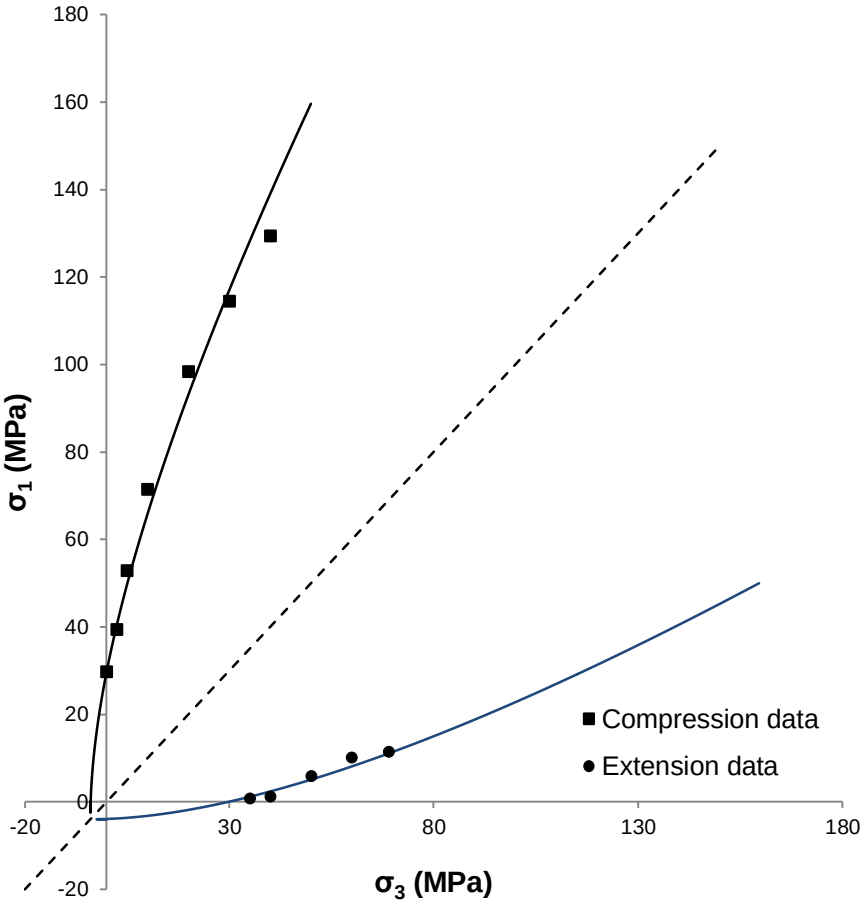

Figure 35: HB $\boldsymbol{\sigma_1}$-$\boldsymbol{\sigma_3}$ fitting

4.4 Stress invariant plane fitting

To fit the MC criterion in the p-q plane the slopes and q-intercepts of the compression and extension lines were calculated:

$$m_c = \frac{6sin\phi}{3 - sin\phi} = \frac{6\sin(28.2)}{3 - \sin(28.2)} = \mathbf{1.12}$$

$$b_c = \frac{6ccos\phi}{3 - sin\phi} = \frac{6 * 8.9 * \cos(28.2)}{3 - \sin(28.2)} = \mathbf{18.6\ MPa}$$

$$m_e = -\frac{6sin\phi}{3 + sin\phi} = \frac{6\sin(28.2)}{3 + \sin(28.2)} = \mathbf{-0.82}$$

$$b_e = -\frac{6c\cos\phi}{3+\sin\phi} = \frac{6 * 8.9 * \cos(28.2)}{3+\sin(28.2)} = \mathbf{-13.6\ MPa}$$

Equations (23) and (24) were then used to plot MC in the p-q plane (Fig. 36). The compression and extension lines intersect the p-axis at the same vertex V_0 calculated from the σ_1-σ_3 plane fitting.

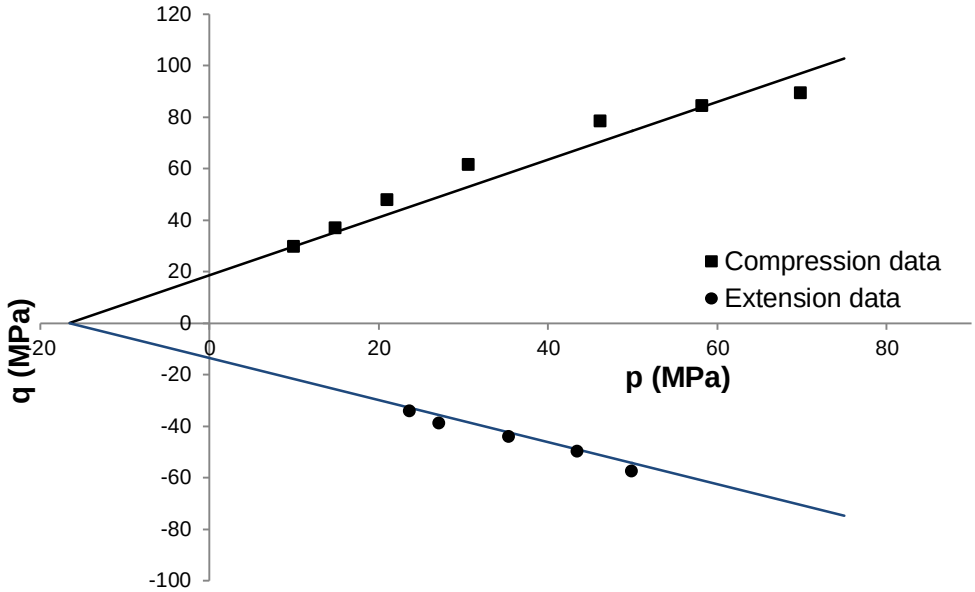

Figure 36: MC p-q plane fitting

To plot the HB criterion in the p-q plane, the strength parameter C_o and fitting parameter *m* found in the σ_1-σ_3 plane were used in equations (41) and (42) (Fig. 37). The HB compression and extension lines intersect the p-axis at the same V_0 as in the σ_1-σ_3 plane. The lines in the p-q plane are nonlinear and are not symmetric about the p-axis.

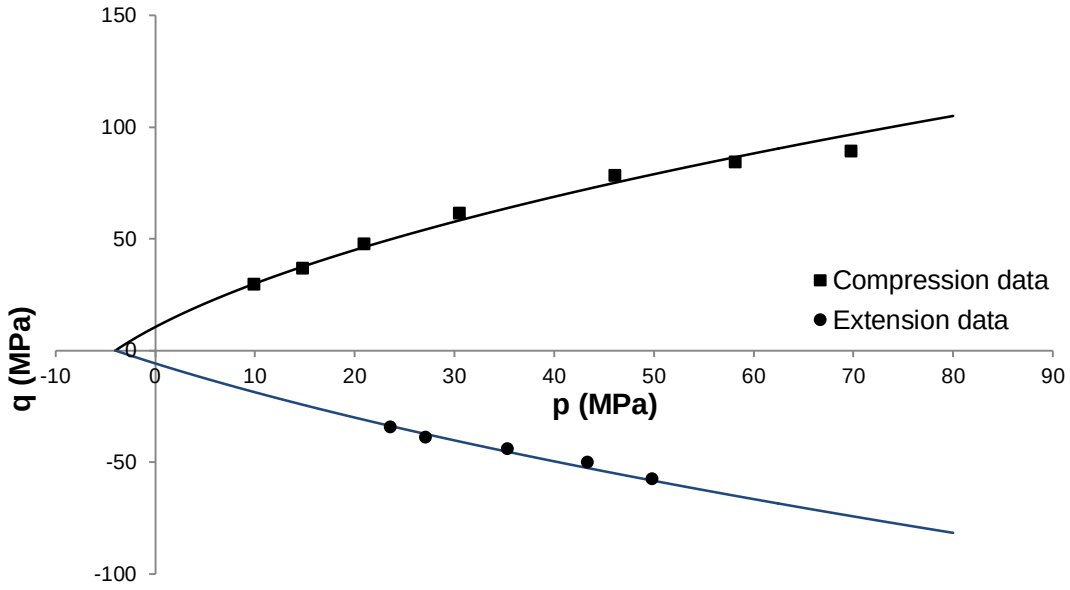

Figure 37: HB p-q plane fitting

Using the method described in chapter two, the PMC criterion was fitted to the compression and extension data in the p-q plane. The least squares solution to the system of equations gave the following constants:

$$A = \frac{b_c}{V_0} = \mathbf{1.03}$$

$$B = k = \mathbf{-0.99}$$

$$C = b_c = \mathbf{24.13\ MPa}$$

The least squares fitting for the compression and extension curve is $R^2 = 0.9784$. From the least squares solution V_0 and b_e are calculated:

$$V_0 = \frac{b_c}{1.03} = \frac{24.13}{1.03} = \mathbf{23.37\ MPa}$$

$$b_e = \frac{b_c}{\alpha} = \frac{b_c}{0.5\left(1 - \sqrt{3}k\right)} = \frac{24.13}{0.5\left(1 - \sqrt{3} * -0.99\right)} = \mathbf{17.78\ MPa}$$

Knowing b_c, b_e, and V_0, the slopes of the compression and extension line are calculated using equation (55):

$$m_c = \frac{b_c}{V_0} = \frac{24.13}{23.37} = \mathbf{1.03}$$

$$m_e = -\frac{b_e}{V_0} = \frac{17.78}{23.37} = \mathbf{-0.76}$$

The strength parameters ϕ_c, ϕ_e, c_c, and c_e can be determined using equations (53) and (54):

$$\phi_c = sin^{-1}\left(\frac{3m_c}{6+m_c}\right) = sin^{-1}\left(\frac{3*1.03}{6+1.03}\right) = \mathbf{26°}$$

$$c_c = \frac{b_c(3-sin\phi_c)}{6cos\phi_c} = \frac{24.13*(3-\sin(26°))}{6\cos(26°)} = \mathbf{11.5\ MPa}$$

$$\phi_e = sin^{-1}\left(\frac{-3m_e}{6+m_e}\right) = sin^{-1}\left(\frac{-3*-0.76}{6-0.76}\right) = \mathbf{26°}$$

$$c_e = \frac{b_e(3+sin\phi_e)}{6cos\phi_e} = \frac{17.78(3+\sin(26))}{6\cos(26)} = \mathbf{11.3\ MPa}$$

With all the strength parameters known, the PMC criterion can be plotted in p-q space (Fig. 38). Although PMC considers the compression and extension data separately, the plot in (Fig. 38) appears similar to MC in (Fig.36). After fitting the data, the friction angles in compression and extension are the same. This means that PMC will give similar results to MC because only one value for friction angle is considered.

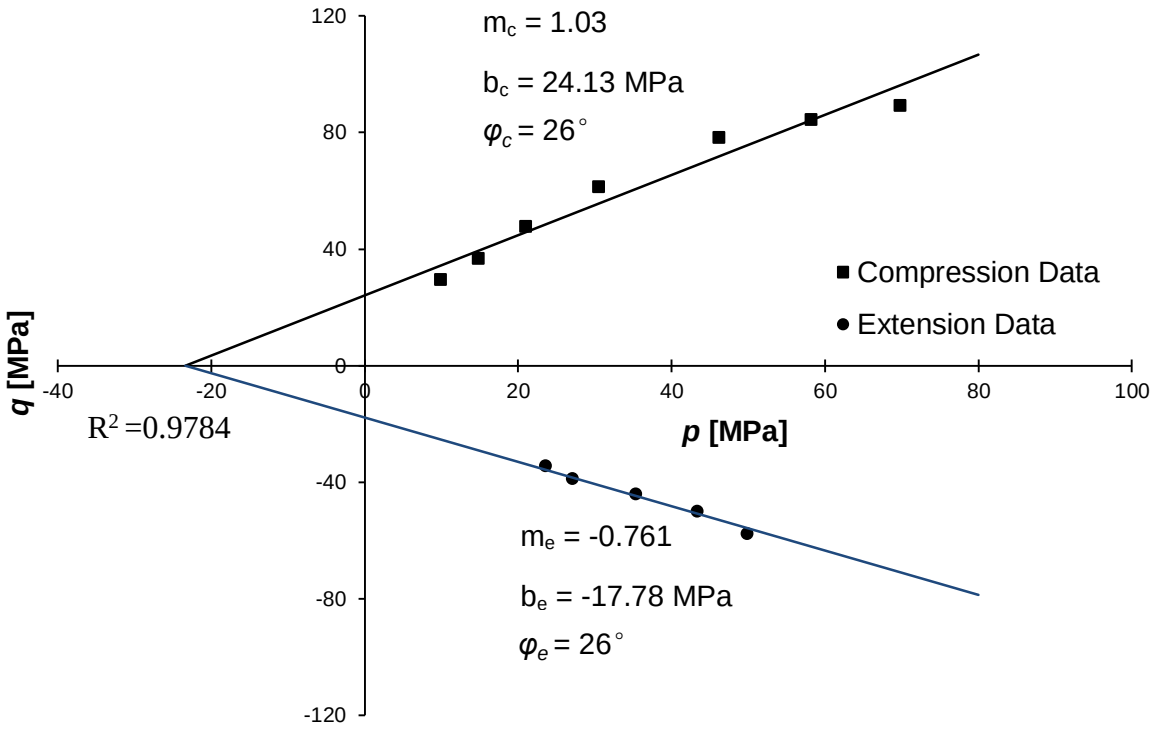

Figure 38: PMC p-q plane fitting

4.5 Pi-plane fitting

The MC criterion is plotted in the π-plane (Fig. 39). The blue data points on the extension and compression axes are the points predicted by the MC criterion. The black data points are multi-axial test results at two different mean stresses. MC is linear in each π-plane section, so a line describing the MC criterion is drawn between the compression and extension point. For a mean stress of p = 28.3 MPa, R^2 = 0.8396. For p = 56.0 MPa, the failure strength is over predicted as the points fall below the MC line.

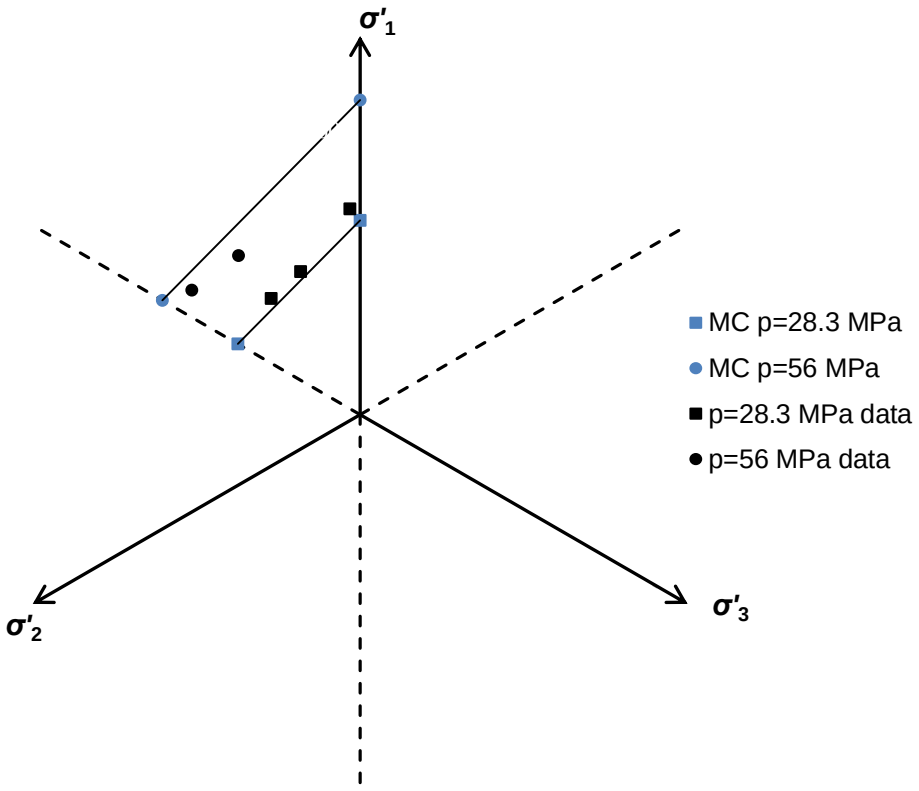

Figure 39: MC pi-plane fitting

The HB criterion is plotted in the π-plane (Fig. 40). Again, the blue points represent the predicted failure in conventional compression and extension. HB is approximately linear in the π-plane, so a line is drawn representing HB failure in the π-plane section. HB predicts failure well at p = 28.3 MPa with at R^2 = 0.9862, but over predicts failure at p = 56.0 MPa.

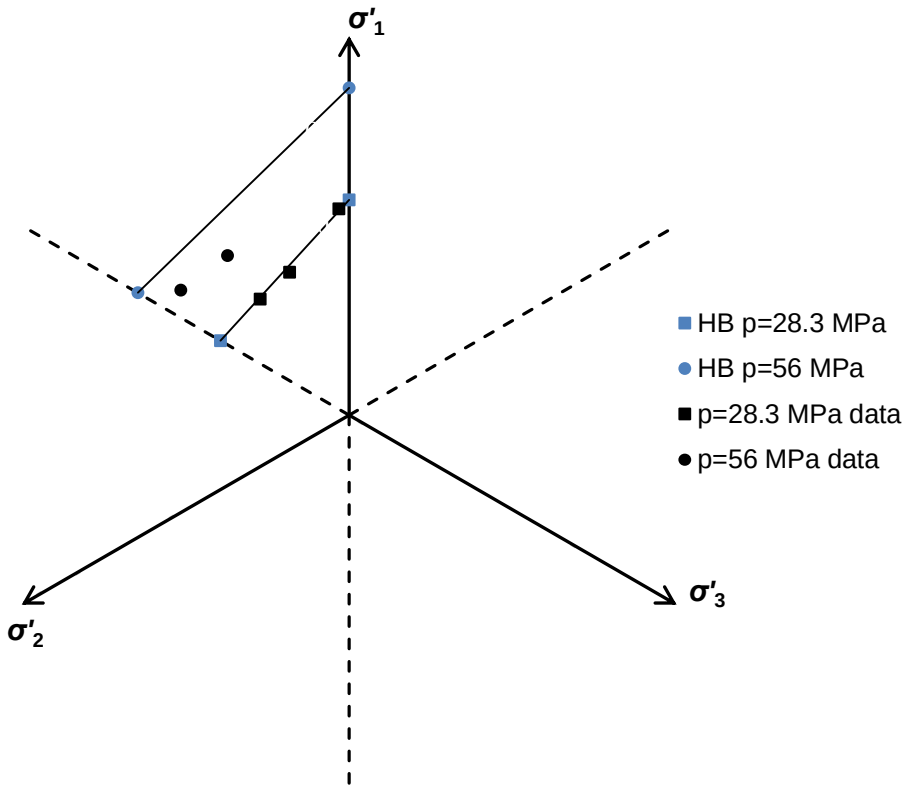

Figure 40: HB pi-plane fitting

PMC is plotted in the π-plane, and the same method as MC and HB is used to construct the failure line (Fig. 41). Failure is predicted well at p = 28.3 MPa with R^2 = 0.9709, but over predicts failure strength at p = 56.0 MPa. PMC accounts for the intermediate principal stress effect on failure strength in the π-plane. However, the friction angle in compression and extension (ϕ_c and ϕ_e) are equal and PMC shows a similar fitting to MC. To optimize this fitting, using a 12-sided PMC failure surface or a plane fitting method may be necessary.

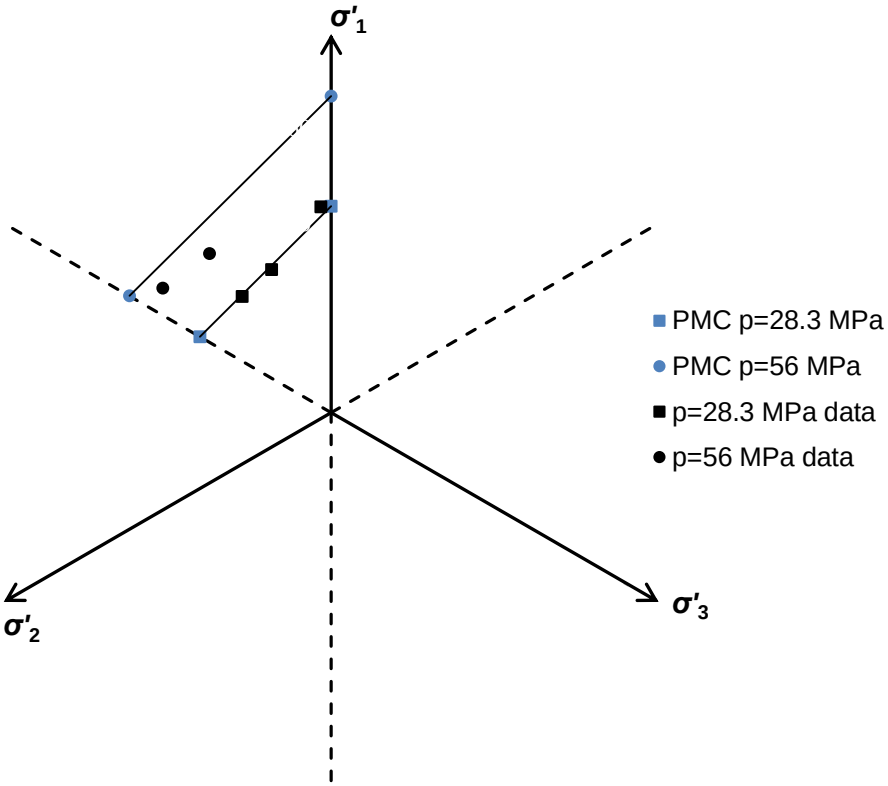

Figure 41: PMC pi-plane fitting

Material parameters are summarized in Table 5 from the fitting of each failure criterion.

Table 5: Material parameters determined from each failure criterion

Failure Criterion	ϕ_c (deg)	ϕ_e (deg)	C_0 (MPa)	c_c (MPa)	c_e (MPa)	m	V_0 (MPa)
MC	28.2	-	29.7	8.9	-	-	16.6
HB	-	-	29.7	-	-	7.5	4.0
PMC	26.0	26.0	29.7	11.5	11.3	-	23.4

Chapter 5: Conclusions

5.1 Summary

A series of experiments were performed on the Dunnville sandstone to evaluate the MC, HB, and PMC failure criteria in different coordinate systems. Each criterion was expressed in different forms to allow for evaluation in the σ_1-σ_3 plane, p-q plane, and π-plane. The failure criteria evaluated are described by several material parameters: the angle of internal friction in compression ϕ_c and extension ϕ_e, vertex V_0, uniaxial compression strength C_0, and a fitting parameter *m*. The material parameters for each criterion were calculated from conventional triaxial compression ($\sigma_{II} = \sigma_{III}$) and extension ($\sigma_I = \sigma_{II}$) results.

To construct a failure surface in any coordinate system, a common vertex V_0 on the tension side of the hydrostatic axis needs to be determined. For the MC and HB criteria V_0 can be calculated directly from the each criterion when expressed in terms of principal stresses. A least squares fitting method was developed for determining V_0 for PMC. By relating the q-intercept in the p-q plane, to the angle θ in the π-plane a system of equations was constructed and solved using conventional triaxial data. V_0 was obtained from the solution to the system of equations.

An area of interest in this thesis was the effect of intermediate stress on failure of the Dunnville sandstone. To investigate this effect, an apparatus was developed to perform multi-axial ($\sigma_1 \neq \sigma_2 \neq \sigma_3$) compression tests. An existing plane strain apparatus was retrofitted with two piston assemblies that control force in the intermediate direction. Design of the apparatus included a 3D finite element model for analysis of shear stress developed within the piston assemblies during experimentation. Calibration was performed to evaluate the force being produced by the assemblies. Plane strain apparatus with piston assemblies installed (true-triaxial apparatus) was used to perform multi-axial experiments.

The true-triaxial apparatus was used to perform multi-axial compression tests at two values of mean stress. A stress path was developed that allowed for constant mean stress testing. By keeping the minor lateral stress constant ($\Delta\sigma_3 = 0$) and keeping the ratio between maintaining the ratio between the major and intermediate stress ($-\Delta\sigma_2 = \Delta\sigma_1$) a constant mean stress condition was obtained. Mean stress was maintained to within a tolerance of ± 0.1 MPa.

Effect of the intermediate principal stress was evaluated by using results obtained from multi-axial testing. A set of coordinate equations was developed for displaying criteria in the π-plane. Results from the multi-axial tests were plotted and compared against each criterion for the two mean stresses tested.

5.2 Future Work

Future work on this subject could involve using the true-triaxial apparatus to perform a plane strain experiment. Traditionally, plane strain testing is performed such that displacement is prevented in the direction of desired plane. However, a plane strain condition is only approximately obtained because the material providing restrain has a finite stiffness. To perform a plane strain experiment with the true-triaxial device could involve monitoring specimen strain in the direction of desired plane strain (ε_2) and increasing/decreasing force in that direction to maintain a constant strain ($\Delta\varepsilon_2 = 0$).

References

Adams, F. D., & Nicolson, J. T. (1901). An experimental investigation into the flow of marble. *Royal Soc. London Philos. Trans. Ser. A, 195*, 597–637.

Davis, R. O., & Selvadurai, A. P. S. (2002). Plasticity and Geomechanics. Cambridge, UK: Cambridge UP.

Drescher, A. (1991). Analytical Methods in Bin Load Analysis. *Amsterdam: Elsevier*

Eberhardt, E. (2012). The Hoek–Brown Failure Criterion. The ISRM Suggested Methods for Rock Characterization, Testing and Monitoring: 2007-2014: 233-40.

Haimson, B., & Chang, C. (2000). A new true triaxial cell for testing mechanical properties of rock, and its use to determine rock strength and deformability of Westerly granite. *International Journal of Rock Mechanics and Mining Sciences 37,* 285-296.

Handin, J., Heard, H. A., & Magouirk, J. N. (1967). Effects of the intermediate principal stress on the failure of limestone, dolomite, and glass at different temperatures and strain rates. *Journal of Geophysical Research 72*, 611-640.

Hojem, J. P. M., & Cook, N. G. W. (1968). The design and construction of a triaxial and polyaxial cell for testing rock specimens. *South African Mechanical Engineering 18*, 57-61.

Hoskins, E. R. (1969). The failure of thick-walled hollow cylinders of isotropic rock. *International Journal of Rock Mechanics and Mining Sciences & Geomechanics 6,* 99-125.

Hunsche, U., & Albrecht, H. (1990). Results of true triaxial strength tests on rock salt. *Engineering Fracture Mechanics 35,* 867-877.

Ingraham, M. D., Issen, K. A., & Holcomb, D, J. (2013). Response of Castlegate sandstone to true triaxial states of stress. *Journal of Geophysical Research: Solid Earth 118,* 536-552.

Labuz, J. F., & Bridell, J. M. (1993). Reducing frictional constraint in compression testing through lubrication. *International journal of rock mechanics, mining sciences, and Geomechanics 30,* 451-455.

Labuz, J. F., Dai, S. T., & Papamichos, E. (1996). Plane-strain Compression of Rock-like Materials. *International Journal of Rock Mechanics, Mining Sciences, and Geomechanics 33,* 573-584.

Labuz, J. F., Vardoulakis, I. G., & Drescher, A. (1991). *U.S. Patent No. 5,063,785.* Washington, DC: U.S. Patent and Trademark Office.

Meyer, J. P. & Labuz, J. F. (2013). Linear failure criteria with three principal stresses. *International Journal of Rock Mechanics and Mining Sciences 60,* 180-187.

Mogi, K. (1969). On a new triaxial compression test of rocks. *In: Abstract 1969 Meeting Seismol.* Soc. Japan, 3.

Mogi, K. (1970). Effect of the triaxial stress system on rock failure. *Rock Mech. in Japan, 1.* 53-55.

Mogi, K. (1977). Dilatancy of rocks under general triaxial stress states with special reference to earthquake precursors. *Journal of Physics of the Earth 25*, 203-217.

Mogi, K. (2007). Experimental rock mechanics. CRC Press.

Morgan, H. S., & Wawersik, W. R. (1991). The Use of Thick-walled Hollow Cylinder Creep Tests For Evaluating Flow Criteria For Rock Salt. *International Society for Rock Mechanics.*

Niwa, Y., Kobayashi, S., & Koyanagi, W. (1967). Failure criterion on lightweight aggregate concrete subjected to triaxial compression. *Mem. Fac. Eng. Kyoto Univ. 29,* 119–131.

Paul, B. (1968). Generalized pyramidal fracture and yield criteria. *International Journal of Solids and Structures 4,* 175-196.

Robertson, E. C. (1955). Experimental study of the strength of rocks. *Geological Society of America Bulletin 66*, 1275-1314.

Takahashi, M. & H. Koide. (1989). Effect of the intermediate principal stress on strength and deformation behavior of sedimentary rocks at the depth shallower than 2000 m. *In: V. Maury and D. Fourmaintraux (eds.), Rock at Great Depth 1,* 19–26.

Wawersik, W. R., Carlson, L. W., Holcomb, D. J., & Williams, R. J. (1997). New Method For True-Triaxial Rock Testing. *International Journal of Rock Mechanics and Mining Sciences 34, Issues 3-4.*